Physics of Fluids

Designing a consistent implementation of the discrete unified gas-kinetic scheme for the simulation of three-dimensional compressible natural convection

Cite as: Phys. Fluids **33**, 046101 (2021); https://doi.org/10.1063/5.0045227
Submitted: 24 January 2021 . Accepted: 15 March 2021 . Published Online: 02 April 2021

Xin Wen (温鑫), Lian-Ping Wang (王连平), and Zhaoli Guo (郭照立)

Physics of Fluids ARTICLE scitation.org/journal/phf

Designing a consistent implementation of the discrete unified gas-kinetic scheme for the simulation of three-dimensional compressible natural convection

Cite as: Phys. Fluids **33**, 046101 (2021); doi: 10.1063/5.0045227
Submitted: 24 January 2021 · Accepted: 15 March 2021 ·
Published Online: 2 April 2021

Xin Wen (温鑫),[1] Lian-Ping Wang (王连平),[1,2,3,a)] and Zhaoli Guo (郭照立)[4]

AFFILIATIONS

[1]Department of Mechanical Engineering, University of Delaware, 126 Spencer Laboratory, Newark, Delaware 19716-3140, USA
[2]Guangdong Provincial Key Laboratory of Turbulence Research and Applications, Center for Complex Flows and Soft Matter Research and Department of Mechanics and Aerospace Engineering, Southern University of Science and Technology, Shenzhen 518055, Guangdong, China
[3]Guangdong-Hong Kong-Macao Joint Laboratory for Data-Driven Fluid Mechanics and Engineering Applications, Southern University of Science and Technology, Shenzhen 518055, China
[4]State Key Laboratory of Coal Combustion, School of energy and Power Engineering, Huazhong University of Science and Technology, Wuhan 430074, Hubei, China

[a)]**Author to whom correspondence should be addressed:** wanglp@sustech.edu.cn

ABSTRACT

Discrete unified gas-kinetic scheme (DUGKS) has been developed as a robust and accurate approach for thermal compressible flow simulations; however, designing an efficient and accurate lattice velocity model to take full advantage of DUGKS remains a challenge. In this study, we apply DUGKS to simulate three-dimensional compressible natural convection in an enclosure with a large temperature difference, without making the Boussinesq approximation. The Chapman–Enskog analysis indicates that the fourth-order moments of equilibrium is needed for the heat flux evaluation in the energy equation, implying that the fourth-order Hermite expansion of equilibrium and thus at least an eighth-order Gauss–Hermite quadrature are needed for accurate simulation of the Navier–Stokes–Fourier system. For this purpose, a highly efficient lattice velocity model, D3Q77A9, is derived, which provides a Gauss–Hermite quadrature of ninth-order accuracy in three dimensions. The accuracy of this D3Q77A9 model is demonstrated by simulating compressible natural convection flows in both two-dimensional and three-dimensional cavities. An error analysis is performed to emphasize the importance of combining a quadrature with an adequate degree of precision and a proper order of Hermite expansion of the equilibrium distribution.

I. INTRODUCTION

In recent years, a number of kinetic methods based on solving a model Boltzmann equation have been developed as an alternative approach in numerical simulation of thermal compressible flows. Instead of solving the Navier–Stokes–Fourier system governing the evolution of the hydrodynamic variables, kinetic methods solve the evolution of the mesoscopic distribution function which relates the microscopic particle dynamics with the macroscopic hydrodynamic variables. Although the model Boltzmann equation is easier to solve when compared to the Navier–Stokes–Fourier system, it also presents unique challenges such as the boundary condition treatment, numerical instability, and proper design of lattice velocity model and quadrature needed to efficiently and accurately evaluate the integral moments of the particle distribution function.

The standard lattice Boltzmann method (LBM) was developed as an efficient and accurate tool to treat incompressible and often isothermal flows at low Mach numbers. Different kinetic models have been proposed for the thermal lattice Boltzmann method: the multispeed approach,[1,2] the hybrid approach,[3,4] and the double-distribution function (DDF) approach.[5–9] In the multispeed approach, by increasing

the number of discrete particle velocities, the compressible Navier–Stokes–Fourier equations can be recovered. In the hybrid approach, the velocity field is simulated by the lattice Boltzmann method, while the temperature field is solved by the conventional CFD method such as a finite-difference or finite-volume method. Solving the macroscopic energy equation with a nonlinear term complicates the numerical process.

As for the DDF approach, there are two types. The first is typically based on the Boussinesq approximation, and the distribution used for temperature is microscopically independent of the distribution used for density and velocity fields. Examples of this type can be found in thermal flow simulations with a small temperature difference.[10–14] The temperature field is treated as a passive scalar which evolves according to the advection-diffusion equation. In the second type, both distributions are derived from the original higher dimensional particle distribution by properly integrating out the internal degrees of freedom, where the first reduced distribution determines density and velocity fields, and the choice for the second reduced distribution is not unique, whose integral may be related to the internal energy,[5,15] total energy,[8,9,16] or partial internal energy.[17,18] Owing to the simplicity in implementation and inner coherence in physics, the DDF model of the second type is widely employed in thermal flow simulations. He *et al.*[5] proposed the first DDF model of the second type which considers both the viscous dissipation and compression work. The temperature field is fully represented by an additional internal energy distribution function, namely, the integral of this second distribution function gives the internal energy $\rho DRT/2$. However, in this method, the evaluation of temperature involves the time and spatial derivatives of the hydrodynamic variables which may introduce some discretization errors. Later on, an alternative thermal DDF model was designed by Guo *et al.*[8] They employed a distribution function for the total energy $\rho(u^2/2 + DRT/2)$ rather than the internal energy. The introduction of this total energy distribution function avoids the calculation of time and spatial derivatives of the hydrodynamic variables. It is worth pointing out that, to simulate compressible natural convection with a large temperature difference, the Hermite expansion of equilibrium distribution function to an appropriate order is needed.[16,19]

Besides LBM, other kinetic methods have been developed rapidly in recent years. The gas-kinetic scheme was developed by Xu.[20] The capability of GKS for thermal flow simulation was first demonstrated by the natural convection flow simulation under the Boussinesq approximation.[11] Recently, Lenz *et al.*[21] performed simulations of compressible natural convection flow, without the Boussinesq approximation; they first investigated two-dimensional unsteady compressible natural convection flows with the Rayleigh number up to 5×10^9. It is worth pointing out that the boundary conditions in GKS are implemented at the macroscopic level. As GKS is limited to the continuum flow, UGKS[22] and DUGKS[17,23] have been developed to treat flows al all Knudsen numbers. Three-dimensional simulations of unsteady natural convection under the Boussinesq approximation were performed by Wang *et al.*[24,25] using DUGKS. Non-uniform meshes can be easily implemented in DUGKS, and results of unsteady convection flows up to $Ra = 10^{10}$ in three dimensional space were provided in the work of Wang *et al.*[25] Laminar to turbulent transition of natural convection in a 3D cubical cavity was studied by Wen *et al.*[14] using DUGKS with an improved implementation of boundary condition. Recently, DUGKS has been extended to two-dimensional simulation of non-Boussinesq type natural convection with a large temperature difference in a square cavity.[18] With these successful implementations, DUGKS is shown to be a reliable simulation tool for thermal flow simulations. Furthermore, as a finite volume method, a non-uniform mesh can be easily employed in DUGKS which is desirable to resolve the sharp temperature and velocity gradients near the walls. For continuum flows, DUGKS can be viewed as a special finite-volume LB scheme, but it is more accurate and robust than FV-LBE.[26] The computational efficiency can be significantly improved with the use of a non-uniform grid.[27,28]

While two-dimensional and three-dimensional simulation results of natural convection in a cavity under the Boussinesq approximation have been studied by different numerical methods,[29,30] compressible natural convection in an enclosure with a large temperature difference is, by far, less explored. Most simulations of the compressible natural convection flows were performed under the low Mach number approximation or solving the steady Navier–Stokes equations.[31–33] Chenoweth and Paolucci[34] performed an early simulation of compressible natural convection. Solving the transient Navier–Stokes equations under the low Mach number approximation, they obtained results of two-dimensional, long-time (i.e., steady), compressible natural convection. Vierendeels *et al.*[32,33] solved two-dimensional steady Navier–Stokes equations and provided solutions for the Rayleigh number range $10^2 \le Ra \le 10^7$ with a temperature difference $\varepsilon = (T_h - T_c)/(2T_0) = 0.6$, where $Ra \equiv 2Pr\varepsilon g H^3 \rho_0^2/(\mu_0^2)$, Pr is the Prandtl number, g is the gravity, ρ_0 is the density at given temperature $T_0 = (T_h + T_c)/2$, μ_0 is viscosity at given temperature, T_h is the temperature of the hot wall, and T_c is the temperature of the cold wall. However, the steady Navier–Stokes equations are not valid for high Rayleigh number convections. For unsteady compressible natural convections, Le Quéré *et al.*[35] studied two-dimensional non-Boussinesq convection in a tall cavity with an aspect ratio $A = 5$ using a Chebyshev collocation algorithm for compressible Navier–Stokes equations under the low Mach number approximation, where $A = H/L$, H is the cavity height, and L is the cavity length. They found that the flow becomes increasingly asymmetrical as the temperature difference is increased, and the critical Rayleigh number also decreases with larger temperature difference. Lenz *et al.*[21] performed two-dimensional compressible natural convection simulations with $Ra = 5.0 \times 10^9$ using the gas-kinetic scheme. Table I summarizes some representative studies of compressible natural convection in an enclosure. The three-dimensional compressible natural convection is rarely explored. In this work, we intend to extend DUGKS to simulate three-dimensional compressible natural convection flows.

There are a few crucial issues we need to resolve in order for DUGKS to simulate three-dimensional natural convection, such as the unity Prandtl number limitation of original BGK model, the order requirement of Gauss–Hermite quadrature in the determination of lattice velocities, and accurate implementation of the boundary condition. According to the analysis of Shan *et al.*,[19] third-order Hermite expansion of equilibrium and quadrature with sixth-degree of precision are required for isothermal flow to recover the Navier–Stokes equations. For compressible flow, the requirements change to a fourth-order Hermite expansion of equilibrium and quadrature at the eighth-degree of precision. In our previous study, we find that the Shakhov model,[17,41] utilized to adjust the Prandtl number, would raise

TABLE I. Studies of compressible natural convection.

	Method	Dimension and resolution	A	Ra
Chenoweth and Paolucci[34]	FD	2D (121×121)	$1-10$	10^3-10^7
Le Quéré *et al.*[35–37]	Spectral	2D $(80 \times 80, 32 \times 96)$	1, 8	$10^5, 10^6$
Vierendeels *et al.*[32,33]	FV	2D (512×512)	1	10^2-10^7
Becker and Braack[38]	FE	2D $(4 \times 10^6$ d.o.f)	1	10^6-10^7
Li *et al.*[39]	LBM	2D (250×250)	1	10^3-10^5
Feng *et al.*[9,40]	LBM	3D $(100 \times 100 \times 10)$	1	10^3-10^5
Lenz *et al.*[21]	GKS	2D (376×376)	1	$10^6, 5 \times 10^9$
Wen *et al.*[18]	DUGKS	2D (360×360)	1	$10^6, 5 \times 10^9$

the requirement of Hermite expansion of equilibrium and the degree of precision of the Gauss–Hermite quadrature. Thus, instead of using the Shakhov model or the Ellipsoidal-Statistical model,[42] we introduce an extra source term to the original BGK model to overcome the unity Prandlt number limitation. In this way, only fourth-order Hermite expansion of the equilibrium and an eighth degree of precision for the quadrature are needed.[19] In our previous work,[18] two-dimensional steady and unsteady compressible natural convection simulations are performed and the results reach an excellent agreement with the literature. For the temperature and velocity boundary condition, we proposed a systematic way of deriving boundary expression based on the Chapman–Enskog expansion, in this way all the nodes at the boundary satisfy the full compressible Navier–Stokes equations.

In DUGKS, particle velocity is discretized into a finite set. For a compressible flow, fourth-order moments of the expanded equilibrium distribution are needed for the heat flux evaluation which requires at least an eighth degree precision of the quadrature. As there is no general theory to construct Gauss quadratures at a given order in multiple spatial dimensions, we use D2Q25A9 model obtained from the production formulas of the D1Q5A9 for previous two-dimensional simulations ($Dn_1Qn_2An_3$ denotes a n_1-dimensional quadrature with n_2 particle velocities having a n_3-degree of quadrature precision). The simply minded extension in this manner would lead to D3Q125A9, which requires 125 discrete velocities in 3D. Shan proposed a general solution of lattice for the LBGK model and provided a D3Q107A9 model.[43,44] As DUGKS does not require discrete velocities to coincide with the mesh, D3Q107A9 model might be too redundant and a more compact model may be designed for DUGKS. In this paper, we will show that it is possible to design a D3Q77A9 model with only 77 discrete velocities. To emphasize the importance of using quadrature with enough degree of precision and equilibrium with adequate order of expansion, we shall perform a series of simulations, along with an error analysis of the simulated flows.

The rest of the paper is organized as follows. The BGK model with a Prandtl number correction term is introduced in Sec. II A, and the derivation of the D3Q77A9 lattice model is shown in Sec. II B. The accuracy of the D3Q77A9 model is validated in Sec. III A and Sec. III B by steady compressible natural convection simulation. An error analysis is given in Sec. III C to show the importance of using appropriate Hermite expansion of the equilibrium and quadrature with enough degree of precision. A brief summary is given in Sec. IV.

II. THE MESOSCOPIC CFD MODEL

A. The gas kinetic model

To recover the fully compressible Navier–Stokes equations, the Boltzmann equation with the Bhatnagar-Gross-Krook (BGK) model is employed in this work.[17] An extra source term S_h is introduced to adjust the system Prandtl number; the detailed derivations of this model are shown in the work of Wen *et al.*[18] and Chen *et al.*[45,46] The system is described by the evolution equations of the two reduced distributions, $g(\boldsymbol{x}, \boldsymbol{\xi}, t)$ and $h(\boldsymbol{x}, \boldsymbol{\xi}, t)$, which depend on the particle velocity $\boldsymbol{\xi}$, space location $\boldsymbol{x}$, and time t, as follows:

$$\frac{\partial g}{\partial t} + \boldsymbol{\xi} \cdot \nabla_x g + \boldsymbol{b} \cdot \nabla_\xi g = \Omega_g = -\frac{g - g^{eq}}{\tau}, \tag{1a}$$

$$\frac{\partial h}{\partial t} + \boldsymbol{\xi} \cdot \nabla_x h + \boldsymbol{b} \cdot \nabla_\xi h = \Omega_h = -\frac{h - h^{eq}}{\tau} + S_h, \tag{1b}$$

$$S_h = \omega(\boldsymbol{\xi}) \left\{ \frac{2(1 - Pr) q_i}{\tau \sqrt{RT_0}} \frac{\xi_i}{\sqrt{RT_0}} \right\}, \tag{1c}$$

where $\boldsymbol{b} = (-g, 0, 0)$ is the body force per unit mass, and the weight function is defined as $\omega(\boldsymbol{\xi}) \equiv \frac{1}{(\sqrt{2\pi RT_0})^D} \exp\left(-\frac{\xi^2}{2RT_0}\right)$. The two equilibrium distributions, g^{eq} and h^{eq}, are given as follows:

$$g^{eq} = \frac{\rho}{(2\pi RT)^{D/2}} \exp\left[-\frac{(\boldsymbol{\xi} - \boldsymbol{u})^2}{2RT}\right], \tag{2a}$$

$$h^{eq} = (K + 3 - D) RT g^{eq}, \tag{2b}$$

where R is gas constant, D is the spatial dimension, and K is the internal degree of freedom. Hydrodynamic variables can be obtained from the moments of the distribution function as

$$\rho = \int g d\boldsymbol{\xi}, \quad \rho \boldsymbol{u} = \int \boldsymbol{\xi} g d\boldsymbol{\xi}, \quad \rho E = \rho(u^2/2 + c_V T) = \frac{1}{2} \int \left(\xi^2 g + h\right) d\boldsymbol{\xi}. \tag{3}$$

The full compressible Navier–Stokes equations can be recovered precisely from the current model. The extra source term S_h is designed to adjust the Prandtl number, contributing only to the heat flux; thus, the continuity equation and momentum equations remain the same. Using the Chapman–Enskog expansion of distribution functions, the heat flux can be written as follows:

$$q_i = \frac{1}{2}\int c_i(c^2 g + h)d\boldsymbol{\xi} = \frac{1}{2}\int c_i c^2 \left\{ g^{eq} - \tau\left[\frac{\partial g^{eq}}{\partial t} + \frac{\partial}{\partial x_j}(\xi_j g^{eq}) + \frac{\partial}{\partial \xi_j}(b_j g^{eq})\right]\right\} d\boldsymbol{\xi} + \frac{1}{2}\int c_i \left\{ h^{eq} + \tau S_h - \tau\left[\frac{\partial h^{eq}}{\partial t} + \frac{\partial}{\partial x_j}(\xi_j h^{eq}) + \frac{\partial}{\partial \xi_j}(b_j h^{eq})\right]\right\} d\boldsymbol{\xi}, \quad (4)$$

where $c_i = \xi_i - u_i$ is the peculiar velocity. Clearly, the fourth-order moments $\int \xi_i\xi_j\xi^2 g^{eq} d\boldsymbol{\xi}$ are needed to evaluate the heat flux, this requires a fourth-order expansion of the equilibrium g^{eq}, $g^{eq,(4)}$, a second-order expansion of the equilibrium h^{eq}, $h^{eq,(2)}$, and at least an eighth degree of precision for the quadrature. The Hermite expansion form of the equilibrium can be written as follows:

$$g^{eq,(4)} = \omega\rho\left\{\begin{array}{l} 1 + \frac{\xi_j u_j}{RT_0} + \frac{1}{2}\left[\frac{(\xi_j u_j)^2}{(RT_0)^2} - \frac{u^2}{RT_0} + (\theta-1)\left(\frac{\xi^2}{RT_0} - D\right)\right] \\ + \frac{1}{6}\frac{\xi_j u_j}{RT_0}\left[\frac{(\xi_j u_j)^2}{(RT_0)^2} - 3\frac{u^2}{RT_0} + 3(\theta-1)\left(\frac{\xi^2}{RT_0} - D - 2\right)\right] \\ + \frac{1}{24}\frac{(\xi_j u_j)^2}{(RT_0)^2}\left[\frac{(\xi_j u_j)^2}{(RT_0)^2} - 6\frac{u^2}{RT_0} + 6(\theta-1)\left(\frac{\xi^2}{RT_0} - D - 4\right)\right] \\ + \frac{1}{8}\frac{u^2}{RT_0}\left[\frac{u^2}{RT_0} + 2(\theta-1)\left(-\frac{\xi^2}{RT_0} + D + 2\right)\right] \\ + \frac{1}{8}(\theta-1)^2\left[\frac{\xi^4}{(RT_0)^2} - (2D+4)\frac{\xi^2}{RT_0} + D^2 + 2D\right] \end{array}\right\} + \mathcal{O}(Ma^5), \quad (5)$$

$$h^{eq,(2)} = \omega\tilde{K}\rho RT\left\{\begin{array}{l} 1 + \frac{\xi_j u_j}{RT_0} + \frac{1}{2}\frac{(\xi_j u_j)^2}{(RT_0)^2} - \frac{1}{2}\frac{u^2}{RT_0} \\ + \frac{1}{2}(\theta-1)\left(\frac{\xi^2}{RT_0} - D\right) \end{array}\right\} + \mathcal{O}(Ma^3), \quad (6)$$

where $\tilde{K} \equiv (K + 3 - D)$ and $\theta \equiv T/T_0$. In DUGKS, the particle velocity space is discretized into a finite set. In the next section, we will show how to design the D3Q77A9 lattice model from D3Q125A9, maintaining the ninth degree of quadrature accuracy.

B. The D3Q77A9 model

In D dimensions, the nth order Hermite polynomial and its weight function can be written as[47]

$$\omega(\boldsymbol{\xi}) = \frac{1}{(2\pi RT_0)^{D/2}}\exp\left(-\frac{\xi^2}{2RT_0}\right), \quad (7a)$$

$$\mathscr{H}^{(n)}(\boldsymbol{\xi}) = (\sqrt{RT_0})^n \frac{(-1)^n}{\omega(\boldsymbol{\xi})}\nabla^n\omega(\boldsymbol{\xi}). \quad (7b)$$

It is important to note that the particle velocity in the weighting function $\omega(\boldsymbol{\xi})$ is scaled by $\sqrt{RT_0}$ based on a fixed reference temperature T_0, so that the discrete velocities to be used for the Gauss–Hermite quadratures are the same for all space locations.

The first few Hermite polynomials are

$$\mathscr{H}^{(0)}(\boldsymbol{\xi}) = 1, \quad (8a)$$

$$\mathscr{H}_i^{(1)}(\boldsymbol{\xi}) = \frac{\xi_i}{\sqrt{RT_0}}, \quad (8b)$$

$$\mathscr{H}_{ij}^{(2)}(\boldsymbol{\xi}) = \frac{\xi_i\xi_j}{RT_0} - \delta_{ij}, \quad (8c)$$

$$\mathscr{H}_{ijk}^{(3)}(\boldsymbol{\xi}) = \frac{\xi_i\xi_j\xi_k}{(\sqrt{RT_0})^3} - \frac{\xi_i}{\sqrt{RT_0}}\delta_{jk} - \frac{\xi_j}{\sqrt{RT_0}}\delta_{ik} - \frac{\xi_k}{\sqrt{RT_0}}\delta_{ij}, \quad (8d)$$

and the recurrence relation of Hermite polynomial is

$$\xi_i\mathscr{H}_{i_1 i_2 \ldots i_n}^{(n)} = \mathscr{H}_{i i_1 i_2 \ldots i_n}^{(n+1)} + \sum_{k=1}^{n}\delta_{i i_k}\mathscr{H}_{i_1 i_2 \ldots i_{k-1} i_{k+2} \ldots i_n}^{(n-1)}. \quad (9)$$

Choosing the orthogonal Hermite polynomials as the expansion basis, the particle distribution function $g(\boldsymbol{x}, \boldsymbol{\xi}, t)$ can be expanded as

$$g \cong g^N \equiv \omega(\boldsymbol{\xi})\sum_{n=0}^{\infty}\frac{1}{n!}\boldsymbol{a}^{(n)}(\boldsymbol{x}, t)\mathscr{H}^{(n)}(\boldsymbol{\xi}), \quad (10)$$

where the rank-n expansion coefficients $\boldsymbol{a}^{(n)}(\boldsymbol{x}, t)$ are given by

$$\boldsymbol{a}^{(n)}(\boldsymbol{x}, t) = \int g(\boldsymbol{x}, \boldsymbol{\xi}, t)\mathscr{H}^{(n)}(\boldsymbol{\xi})d\boldsymbol{\xi}, \quad (11)$$

where the first few expansion coefficients are hydrodynamic variables. For example, $a^{(0)} = \int f d\boldsymbol{\xi} = \rho, a^{(1)} = \int f\xi_i d\boldsymbol{\xi} = \rho u_i$. The mutual orthogonality of the Hermite polynomials allows us to approximate the distribution function up to Nth order by truncating higher-order terms in its Hermite expansion. Namely, a distribution function g can

be approximated by its truncated Hermite expansion g^N, up to order N, without changing all the moments up to the Nth order. Then the expansion coefficient can be rewritten as

$$\boldsymbol{a}^{(n)} = \int g^N \mathscr{H}^{(n)}(\boldsymbol{\xi}) d\boldsymbol{\xi} \equiv \int \omega(\boldsymbol{\xi}) p(\boldsymbol{x}, \boldsymbol{\xi}, t) d\boldsymbol{\xi}, \tag{12}$$

where $p(\boldsymbol{x}, \boldsymbol{\xi}, t)$ is a polynomial of $\boldsymbol{\xi}$ of a degree not greater than $2N$. In DUGKS, the particle velocity space is discretized and Gauss–Hermite quadrature is employed for an accurate moment evaluation

$$\int \omega(\boldsymbol{\xi}) p(\boldsymbol{x}, \boldsymbol{\xi}, t) d\boldsymbol{\xi} = \sum_{a=1}^{d} \omega_a p(\boldsymbol{x}, \boldsymbol{\xi}_a, t), \tag{13}$$

where $\boldsymbol{\xi}_a$ and ω_a are abscissa and weights of a Gauss–Hermite quadrature of a degree $\leq 2N$. In one dimension, the orthogonal polynomials of the Gauss–Hermite quadrature are Hermite polynomials, and the abscissae of the d-point Gauss–Hermite quadrature are the zeros of $\mathscr{H}^{(d)}$. The corresponding weights are

$$\omega_\alpha = \frac{d!}{\left[d\mathscr{H}^{(d-1)}(\xi_\alpha)\right]^2}. \tag{14}$$

In one dimension, d-point quadrature has $(2d-1)$ degree of precision. Table II shows the ninth-order Gauss–Hermite quadrature model D1Q5A9, where $c_0 = \sqrt{RT_0}$. Three dimensional ninth-order quadrature D3Q125A9 obtained from the production formulas, based on D1Q5A9, is shown in Table III.

Shan[43,44] proposed a general procedure to design a Cartesian LBGK lattice at a given degree of quadrature order, with abscissas the weights solved from the following equations

$$\sum_{\alpha=1}^{d} w_\alpha \mathscr{H}^{(n)}(\boldsymbol{\xi}_\alpha) = \begin{cases} 1 & n = 0 \\ 0 & n \neq 0 \end{cases}, \quad \forall n \leq Q. \tag{15}$$

The equation above is the necessary and sufficient condition for any Hermite quadrature to have degree precision of Q regardless of whether the abscissas fall on a Cartesian grid or not. In one dimension, $Q = 2d-1$, as $2d$ independent constraints can be established for $n = 0, 1, 2, \ldots, (2d-1)$.

Now consider D3Q125A9 with $Q = 9$. Our strategy is to use the same discrete particle velocity components, but re-design the weighting factors w_α in order to eventually reduce the actual number of particle velocities, without changing Q. First, we note that the weighting factors are all positive and only depend on the magnitude of the particle velocity (or the particle speed), namely, one weight factor is associated with each group. All odd-n equations are automatically satisfied due to internal symmetries within each group. Based on Eq. (15), we

TABLE II. One-dimensional Gauss–Hermite quadrature D1Q5A9.

Quadrature	ξ_α	ω_α
D1Q5A9	0	8/15
	$\pm\left(\sqrt{5+\sqrt{10}}\right)c_0$	$\left(7-2\sqrt{10}\right)/60$
	$\pm\left(\sqrt{5-\sqrt{10}}\right)c_0$	$\left(7+2\sqrt{10}\right)/60$

TABLE III. Three-dimensional Gauss–Hermite quadrature D3Q125A9. p is the number of discrete velocities in each group. Only the magnitude of the velocity components is indicated in each group, and the combination can be arbitrarily rearranged over the three space directions.

Group	ξ_α	p	ω_α	
1	$(0, 0, 0)$	1	512/3375	
2	$(r, 0, 0)$	6	$16\left(7-2\sqrt{10}\right)/3375$	$r^2 = \left(5+\sqrt{10}\right)c_0^2$
3	$(s, 0, 0)$	6	$16\left(7+2\sqrt{10}\right)/3375$	$s^2 = \left(5-\sqrt{10}\right)c_0^2$
4	$(r, r, 0)$	12	$\left(89-28\sqrt{10}\right)/6750$	
5	$(s, s, 0)$	12	$\left(89+28\sqrt{10}\right)/6750$	
6	$(r, s, 0)$	24	1/750	
7	(r, r, s)	24	$\left(7-2\sqrt{10}\right)/24\,000$	
8	(s, s, r)	24	$\left(7+2\sqrt{10}\right)/24000$	
9	(r, r, r)	8	$\left(1183-374\sqrt{10}\right)/216\,000$	
10	(s, s, s)	8	$\left(1183+374\sqrt{10}\right)/216\,000$	

can obtain 11 constraints from the D3Q125A9 model, which are stated below for the ten weighting factors. These even-n equations can be easily constructed with the help of the non-zero polynomials listed below, and the parameters are obtained by hand calculations.

For $n = 0$, $\mathscr{H}^{(0)} = 1$,

$$w_1 + 6(w_2 + w_3) + 12(w_4 + w_5) + 24(w_6 + w_7 + w_8) + 8(w_9 + w_{10}) = 1. \tag{16}$$

For $n = 2$, $\mathscr{H}^{(2)}_{xx} = x^2 - 1$,

$$\begin{aligned} &-w_1 + (2r^2-6)w_2 + (2s^2-6)w_3 + (8r^2-12)w_4 + (8s^2-12)w_5 \\ &+ (8r^2+8s^2-24)w_6 + (16r^2+8s^2-24)w_7 \\ &+ (16s^2+8r^2-24)w_8 + 8(r^2-1)w_9 + 8(s^2-1)w_{10} = 0. \end{aligned} \tag{17}$$

For $n = 4$, there are two independent Hermite polynomial configurations as far as the condition for the weighting coefficients. The first is $\mathscr{H}^{(4)}_{xxxx} = x^4 - 6x^2 + 3$, which yields

$$\begin{aligned} &3w_1 + (2r^4-12r^2+18)w_2 + (2s^4-12s^2+18)w_3 \\ &+ (8r^4-48r^2+36)w_4 + (8s^4-48s^2+36)w_5 \\ &+ (8r^4-48r^2+8s^4-48s^2+72)w_6 \\ &+ \left[16(r^4-6r^2) + 8(s^4-6s^2) + 72\right]w_7 \\ &+ \left[16(s^4-6s^2) + 8(r^4-6r^2) + 72\right]w_8 \\ &+ 8(r^4-6r^2+3)w_9 + 8(s^4-6s^2+3)w_{10} = 0. \end{aligned} \tag{18}$$

The second is $\mathscr{H}^{(4)}_{xxyy} = x^2y^2 - (x^2+y^2) + 1$, giving

$$\begin{aligned} &w_1 + (-4r^2+6)w_2 + (-4s^2+6)w_3 + 4(r^4-4r^2+3)w_4 \\ &+ 4(s^4-4s^2+3)w_5 + 8\left[r^2s^2 - 2(r^2+s^2) + 3\right]w_6 \\ &+ 8\left[r^4 + 2r^2s^2 - 2(2r^2+s^2) + 3\right]w_7 \\ &+ 8\left[s^4 + 2r^2s^2 - 2(2s^2+r^2) + 3\right]w_8 \\ &+ 8(r^4-2r^2+1)w_9 + 8(s^4-2s^2+1)w_{10} = 0. \end{aligned} \tag{19}$$

At $n = 6$, three independent Hermite polynomial configurations can be identified. The first one, $\mathscr{H}^{(6)}_{xxxxxx} = x^6 - 15x^4 + 45x^2 - 15$, yields

$$-15w_1+\left[2(r^6-15r^4+45r^2)-90\right]w_2+\left[2(s^6-15s^4+45s^2)-90\right]w_3+\left[8(r^6-15r^4+45r^2)-180\right]w_4+\left[8(s^6-15s^4+45s^2)-180\right]w_5$$
$$+\left[8(r^6-15r^4+45r^2)+8(s^6-15s^4+45s^2)-360\right]w_6+\left[16(r^6-15r^4+45r^2)+8(s^6-15s^4+45s^2)-360\right]w_7$$
$$+\left[8(r^6-15r^4+45r^2)+16(s^6-15s^4+45s^2)-360\right]w_8+8(r^6-15r^4+45r^2-15)w_9+8(s^6-15s^4+45s^2-15)w_{10}=0. \quad (20)$$

The second one, $\mathscr{H}^{(6)}_{xxxxyy}=x^4y^2-(x^4+6x^2y^2)+(6x^2+3y^2)-3$, leads to

$$-3w_1+\left[2(-r^4+9r^2)-18\right]w_2+\left[2(-s^4+9s^2)-18\right]w_3+4(r^6-8r^4+18r^2-9)w_4+4(s^6-8s^4+18s^2-9)w_5$$
$$+\left[4(r^4s^2+s^4r^2)-8(r^4+s^4+6r^2s^2)+72(r^2+s^2)-72\right]w_6+\left[8(r^6+r^4s^2+s^4r^2)-8(8r^4+s^4+12r^2s^2)+72(2r^2+s^2)-72\right]w_7$$
$$+\left[8(s^6+r^4s^2+s^4r^2)-8(8s^4+r^4+12r^2s^2)+72(2s^2+r^2)-72\right]w_8+8(r^6-7r^4+9r^2-3)w_9+8(s^6-7s^4+9s^2-3)w_{10}=0. \quad (21)$$

The third one, $\mathscr{H}^{(6)}_{xxyyzz}=x^2y^2z^2-(x^2y^2+x^2z^2+y^2z^2)+(x^2+y^2+z^2)-1$, gives

$$-1w_1+6(r^2-1)w_2+6(s^2-1)w_3+12(-r^4+2r^2-1)w_4+12(-s^4+2s^2-1)w_5+24(-r^2s^2+r^2+s^2-1)w_6$$
$$+24\left[r^4s^2-(r^4+2r^2s^2)+(2r^2+s^2)-1\right]w_7+24\left[s^4r^2-(s^4+2r^2s^2)+(2s^2+r^2)-1\right]w_8$$
$$+8(r^6-3r^4+3r^2-1)w_9+8(s^6-3s^4+3s^2-1)w_{10}=0. \quad (22)$$

Finally, at $n=8$, 4 independent Hermite polynomial configurations exist. The first one, $\mathscr{H}^{(8)}_{xxxxxxxx}=x^8-28x^6+210x^4-420x^2+105$, leads to

$$105w_1+\left[2(r^8-28r^6+210r^4-420r^2)+630\right]w_2+\left[2(s^8-28s^6+210s^4-420s^2)+630\right]w_3+\left[8(r^8-28r^6+210r^4-420r^2)+1260\right]w_4$$
$$+\left[8(s^8-28s^6+210s^4-420s^2)+1260\right]w_5+\left[8(r^8-28r^6+210r^4-420r^2)+8(s^8-28s^6+210s^4-420s^2)+2520\right]w_6$$
$$+\left[16(r^8-28r^6+210r^4-420r^2)+8(s^8-28s^6+210s^4-420s^2)+2520\right]w_7+\left[8(r^8-28r^6+210r^4-420r^2)+16(s^8-28s^6\right.$$
$$\left.+210s^4-420s^2)+2520\right]w_8+8(r^8-28r^6+210r^4-420r^2+105)w_9+8(s^8-28s^6+210s^4-420s^2+105)w_{10}=0. \quad (23)$$

The second one, $\mathscr{H}^{(8)}_{xxxxxxyy}=x^6y^2-(x^6+15x^4y^2)+15(x^4+3x^2y^2)-(45x^2+15y^2)+15$, yields

$$15w_1+(-2r^6+30r^4-120r^2+90)w_2+(-2s^6+30s^4-120s^2+90)w_3+\left[4(r^8-17r^6+75r^4-120r^2)+180\right]w_4$$
$$+\left[4(s^8-17s^6+75s^4-120s^2)+180\right]w_5+4\begin{bmatrix}(r^6s^2+s^6r^2)-(2r^6+2s^6+15r^4s^2+15r^2s^4)\\+30(r^4+s^4+3r^2s^2)-120(r^2+s^2)+90\end{bmatrix}w_6$$
$$+8\begin{bmatrix}(r^8+r^6s^2+s^6r^2)-(17r^6+s^6+15r^4s^2+15s^4r^2)\\+15(5r^4+s^4+6r^2s^2)-60(2r^2+s^2)+45\end{bmatrix}w_7+8\begin{bmatrix}(s^8+r^6s^2+s^6r^2)-(17s^6+r^6+15r^4s^2+15s^4r^2)\\+15(5s^4+r^4+6r^2s^2)-60(2s^2+r^2)+45\end{bmatrix}w_8$$
$$+8(r^8-16r^6+60r^4-60r^2+15)w_9+8(s^8-16s^6+60s^4-60s^2+15)w_{10}=0. \quad (24)$$

The third one, $\mathscr{H}^{(8)}_{xxxxyyyy}=x^4y^4-6(x^4y^2+x^2y^4)+(3x^4+3y^4+36x^2y^2)-18(x^2+y^2)+9$, provides

$$9w_1+(12r^4-72r^2+54)w_2+(12s^4-72s^2+54)w_3+4[r^8-12r^6+48r^4-72r^2+27]w_4+4[s^8-12s^6+48s^4-72s^2+27]w_5$$
$$+8\left[r^4s^4-6(r^4s^2+r^2s^4)+6(r^4+s^4+6r^2s^2)-36(r^2+s^2)+27\right]w_6+8\begin{bmatrix}(r^8+2r^4s^4)-12(r^6+r^4s^2+r^2s^4)\\+6(8r^4+s^4+12r^2s^2)-36(2r^2+s^2)+27\end{bmatrix}w_7$$
$$+8\begin{bmatrix}(s^8+2r^4s^4)-12(s^6+r^4s^2+r^2s^4)\\+6(8s^4+r^4+12r^2s^2)-36(2s^2+r^2)+27\end{bmatrix}w_8+8(r^8-12r^6+42r^4-36r^2+9)w_9+8(s^8-12s^6+42s^4-36s^2+9)w_{10}=0., \quad (25)$$

The last one, $\mathscr{H}^{(8)}_{xxxxyyzz}=x^4y^2z^2-(x^4y^2+x^4z^2+6x^2y^2z^2)+(x^4+6x^2y^2+6x^2z^2+3y^2z^2)-(6x^2+3y^2+3z^2)+3$, leads to

$$3w_1+(2r^4-24r^2+18)w_2+(2s^4-24s^2+18)w_3+4(-2r^6+17r^4-24r^2+9)w_4+4(-2s^6+17s^4-24s^2+9)w_5$$
$$+\left[-8(r^4s^2+s^4r^2)+8(r^4+s^4+15r^2s^2)-96(r^2+s^2)+72\right]w_6+\begin{bmatrix}8(2r^6s^2+r^4s^4)-16(r^6+10r^4s^2+s^4r^2)\\+8(17r^4+s^4+30r^2s^2)-96(2r^2+s^2)+72\end{bmatrix}w_7$$
$$+\begin{bmatrix}8(2s^6r^2+s^4r^4)-16(s^6+10s^4r^2+r^4s^2)\\+8(17s^4+r^4+30s^2r^2)-96(2s^2+r^2)+72\end{bmatrix}w_8+8(r^8-8r^6+16r^4-12r^2+3)w_9$$
$$+8(s^8-8s^6+16s^4-12s^2+3)w_{10}=0. \quad (26)$$

Together, there are 11 equations, forming a linear system for the 10 parameters w_α. However, they are not all independent. With the help of the Matlab function, we determine that the rank of the above system is actually 8. This fact implies that we have an under-determined linear system

to solve, and there are many possibilities for assigning the coefficients. For the best computational efficiency, we decided to eliminate two vector groups with the largest degree (24) of freedom in each, namely, groups 7 and 8 (see Table III). It is rather fortunate that the new system with only 8 vector groups can lead to a linear system with a rank equal to eight and as such the weighting factors can now be uniquely determined. Table IV shows the resulting 77 abscissas and their corresponding weights. To further confirm the degree precision of our D3Q77A9 model, we substitute the newly obtained abscissas and their corresponding weights into the general equation, Eq. (15), as shown in Appendix A. It is shown that 11 required conditions for the 9th-order quadrature accuracy are indeed satisfied. It is interesting to note that, in the resulting model, $w_4 = w_7$ and $w_5 = w_8$, the exact reason for these two identities is not clear to us. It is worth pointing out that the D3Q77A9 model is only one of many possible simplifications of the D3Q25A9 model. Other choices of eliminating vector groups lead to different simplifications of the D3Q125A9 model. In Appendix C, we provide a few other possible choices of simplified quadrature models. As an additional note, we point out that the D2Q25A9 cannot be further optimized by following the above procedure. The condition, Eq. (15) for D2Q25A9, would involve 6 number of independent vector groups and lead to a linear system with a rank equation to 6.

C. Implementation of the kinetic boundary conditions

For our current study, we have no-slip velocity boundary conditions for all walls. The thermal boundary conditions include two adiabatic walls of zero heat flux and two isothermal walls of a given temperature. The velocity field is determined by the distribution $g(\boldsymbol{\xi}_\alpha, \boldsymbol{x}, t)$, while the temperature field is related to both $g(\boldsymbol{\xi}, \boldsymbol{x}, t)$ and $h(\boldsymbol{\xi}_\alpha, \boldsymbol{x}, t)$; thus, it is more complex to perform the kinetic treatment (i.e., in terms of g and h) of the macroscopic boundary conditions. The kinetic treatment of boundary conditions can be derived systematically based on the Chapman–Enskog analysis. The details of the derivation are presented in the work of Wen *et al.*[18] The no-slip velocity condition is accomplished by the following relation:

$$g(\xi_{a,j}, t) = g(\xi_{\bar{a},j}, t) - \tau W_a \rho_w \frac{\xi_{a,j}}{T_0}\frac{\partial T}{\partial x_j} \times \left\{ \begin{array}{l} \left(\frac{\xi_a^2}{RT_0} - D - 2\right) \\ \frac{1}{2}(\theta-1)\left[\frac{\xi_a^4}{(RT_0)^2} - 2(D+3)\frac{\xi_a^2}{RT_0} + (D+2)^2\right] \\ \frac{1}{8}(\theta-1)^2\left[\frac{\xi_a^6}{(RT_0)^3} - (3D+14)\frac{\xi_a^4}{(RT_0)^2} + (D+4)(3D+10)\frac{\xi_a^2}{(RT_0)} - (D+2)^2(D+4)\right] \end{array} \right\} + \mathcal{O}(\tau^2, Ma^5), \quad (27)$$

where $\xi_{a,j}$ denotes the particles bouncing back from the wall and $\xi_{\bar{a},j} = -\xi_{a,j}$. $g(\xi_{\bar{a},j}, t)$ at the wall interface node are typically known at the end of the time step. The normalized temperature is defined as $\theta = T_w/T_0$, and ρ_w and T_w are density and temperature at the wall node, respectively. For the adiabatic walls, the normal temperature gradient is zero, $\partial T/\partial n = 0$. Temperature gradients in the tangential direction are approximated from the temperature values at the previous time step by finite-difference. For the two isothermal walls, $T_w = T_h$ or $T_w = T_c$ is applied, and then the temperature gradient in tangential direction is zero; the normal temperature gradient is approximated with values at the previous time step by finite-difference.

TABLE IV. Three-dimensional quadrature D3Q77A9.

Group	ξ_α	p	ω_α	
1	$(0,0,0)$	1	$1.214\,814\,81 \times 10^{-1}$	
2	$(r,0,0)$	6	$9.194\,665\,02 \times 10^{-4}$	$r^2 = (5+\sqrt{10})c_0^2$
3	$(s,0,0)$	6	$8.056\,201\,49 \times 10^{-2}$	$s^2 = (5-\sqrt{10})c_0^2$
4	$(r,r,0)$	12	$4.224\,310\,33 \times 10^{-5}$	
5	$(s,s,0)$	12	$1.643\,923\,84 \times 10^{-2}$	
6	$(r,s,0)$	24	$2.500\,000\,00 \times 10^{-3}$	
7	(r,r,r)	8	$4.224\,310\,33 \times 10^{-5}$	
8	(s,s,s)	8	$1.643\,923\,84 \times 10^{-2}$	

For the adiabatic boundary condition, the $h(\boldsymbol{\xi}_\alpha, \boldsymbol{x}, t)$ distribution function is treated by

$$h(\xi_{a,j}, t) = h(\xi_{\bar{a},j}, t) - \tilde{K}\rho R\tau W_a \xi_{a,j}\frac{\partial T}{\partial x_j}\left\{\left(\frac{\xi_a^2}{RT_0} - D\right) + \frac{1}{2}(\theta-1)\left[\frac{\xi_a^4}{(RT_0)^2} - 2(D+1)\frac{\xi_a^2}{RT_0} + D^2\right]\right\} + 2W_a\frac{2(1-Pr)}{\sqrt{RT_0}}\frac{\boldsymbol{\xi}_a \cdot \boldsymbol{q}}{\sqrt{RT_0}} + \mathcal{O}(\tau^2, Ma^3), \quad (28)$$

where $\tilde{K} \equiv (K+3-D)$. Zero heat flux $q_z = 0$ and $\partial T_w/\partial z = 0$ are enforced on the top and bottom adiabatic walls. Heat flux in the tangential direction q_x can be approximated by the heat flux value at previous time step $q_x^{(n-1)} = \frac{1}{2}\int c_x(c^2 g^{(n-1)} + h^{(n-1)})d\boldsymbol{\xi}$. Temperature gradient in the tangential direction is also calculated by the values from the last time step by finite difference.

Finally, for the two vertical isothermal walls, the following relationship is used for $h(\boldsymbol{\xi}_\alpha, \boldsymbol{x}, t)$:

$$h(\xi_{a,j}) = -h(\xi_{\bar{a},j}) + 2W_a\tilde{K}p\left[1 + \frac{1}{2}(\theta-1)\left(\frac{\xi_a^2}{RT_0} - D\right)\right] + 2\tau W_a\tilde{K}p\frac{\partial u_j}{\partial x_j} \times \left[\begin{array}{l}(2-\theta)\frac{\xi_a^2}{(K+3)RT_0} + \frac{\tilde{K}+2}{K+3} \\ + \frac{1}{2}(\theta-1)\left(\frac{\xi_a^2}{RT_0} - D\right)\left(\frac{\xi_a^2}{(K+3)RT_0} + \frac{\tilde{K}+2}{K+3}\right)\end{array}\right] + 2\tau W_a\tilde{K}p\frac{\xi_{a,i}\xi_{a,j}}{RT_0}\frac{\partial u_i}{\partial x_j}\left[\theta - 2 - \frac{1}{2}(\theta-1)\left(\frac{\xi_a^2}{RT_0} - D\right)\right] + \mathcal{O}(\tau^2, Ma^3), \quad (29)$$

where $T_w = T_h$ or $T_w = T_c$ is applied at hot and cold wall, respectively. As the no-slip boundary condition is enforced, the velocity gradient $\partial \boldsymbol{u}/\partial z = 0$ is set to zero. The velocity gradients $\partial \boldsymbol{u}/\partial x$ are approximated from velocities values at previous time step by finite-difference. It is worth pointing out that we retain all the $\mathcal{O}(\tau)$ terms to have an accuracy up to $\mathcal{O}(\tau)$. Besides, to be consistent with the Hermite expansion of equilibrium distribution, the temperature $1/T$ is expanded to the order of $\mathcal{O}(Ma^4)$. The standard 'bounce-back' and 'anti-bounce-back' in LBM can be recovered from the above kinetic boundary conditions for isothermal flows.

III. RESULTS AND DISCUSSION

To validate the accuracy of our newly designed D3Q77A9 model, we perform simulations of compressible natural convection which requires at least eighth-order accuracy in the Gauss–Hermite quadrature. Although D3Q77A9 model is more compact compared to D3Q107A9, it still requires a significant computational resource for three-dimensional simulations. Here we primarily consider a two-dimensional natural convection flow problem using a three-dimensional code. Preliminary simulation results of three-dimensional natural convection in a cubical cavity will also be reported in Sec. III B.

A. Steady compressible natural convection

An air-filled ($Pr = 0.71$) square cavity is considered. It is heated on the left by holding the temperaure at $T_h = T_0(1+\varepsilon)$ and cooled on the right by fixing temperature at $T_c = T_0(1-\varepsilon)$. The top and bottom walls are adiabatic as shown in Fig. 1. The coordinate system used is as follows: z is the vertical direction, x is the horizontal direction perpendicular to the heated wall, and y is the spanwise direction. The aspect ratio of the cavity is $A = H/L = 1$. There are only two nodes in the y-direction and the periodic condition is applied in the y-direction, these together imply that there is no variation in y and as such the convection flow is two dimensional. The two dimensional setting allows us here to study systematically various combinations of the details in the mesoscopic model.

The governing equations for the current problem are the compressible Navier–Stokes equations

$$\frac{\partial \rho}{\partial t} + \frac{\partial (\rho u_j)}{\partial x_j} = 0, \tag{30a}$$

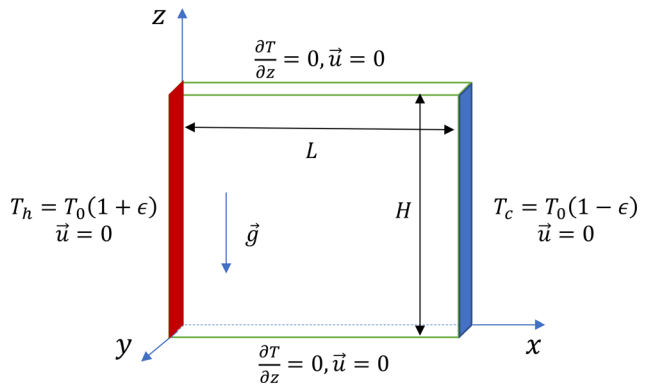

FIG. 1. The geometry under consideration.

$$\frac{\partial (\rho u_i)}{\partial t} + \frac{\partial (\rho u_i u_j)}{\partial x_j} = -\frac{\partial p}{\partial x_i} + \rho g_i + \frac{\partial \sigma_{ij}}{\partial x_j}, \tag{30b}$$

$$\frac{\partial (\rho C_V T)}{\partial t} + \frac{\partial (\rho u_j C_V T)}{\partial x_j} = -p\frac{\partial u_j}{\partial x_j} + \frac{\partial}{\partial x_j}\left(k\frac{\partial T}{\partial x_j}\right) + \sigma_{ij}\frac{\partial u_j}{\partial x_j}, \tag{30c}$$

$$p = \rho R T, \tag{30d}$$

where the stress tensor is $\sigma_{ij} = 2\mu\left(S_{ij} - \frac{1}{D}\nabla\cdot\boldsymbol{u}\delta_{ij}\right) + \mu^V \nabla\cdot\boldsymbol{u}\delta_{ij}$, S_{ij} is the strain rate tensor, and μ and μ^V are the shear viscosity and the bulk viscosity, respectively. When we have a large temperature difference, the fluid properties could vary as a function of the local temperature. The viscosity is given by Sutherland's law

$$\frac{\mu(T)}{\mu^*} = \left(\frac{T}{T^*}\right)^{3/2}\frac{T^*+S}{T+S}, \quad k(T) = \frac{\mu(T)C_p}{Pr}, \tag{31}$$

where $T^* = 273K$, $S = 110.5K$. The viscosity at a reference temperature, $T_0 = (T_h + T_c)/2$, $\mu_0 = \mu(T_0)$, is then calculated by $\mu^* = \mu_0[(T/T^*)^{3/2} \times (T^*+S)/(T+S)]^{-1}$. Note here that $T^* = 273\,K$ is a parameter used in Sutherland's law, and $T_0 = 600\,K$ is the reference temperature used in our problem setup.

To normalize the governing equation, we introduce the following reference scales: the density scale ρ_0, the velocity scale $u_0 = \sqrt{(T_h - T_c)gH/T_0}$, the length scale H, the timescale H/u_0, and the temperature scale T_0. the viscosity is normalized by $\mu_0 = \mu(T_0)$, and the reference heat conductivity is $k_0 = k(T_0)$. The dimensionless governing equations of compressible natural convection can be written as

$$\frac{\partial \hat{\rho}}{\partial \hat{t}} + \frac{\partial (\hat{\rho}\hat{u}_j)}{\partial \hat{x}_j} = 0, \tag{32a}$$

$$\frac{\partial (\hat{\rho}\hat{u}_i)}{\partial \hat{t}} + \frac{\partial (\hat{\rho}\hat{u}_i\hat{u}_j)}{\partial \hat{x}_j} = -\frac{\partial \hat{p}}{\partial \hat{x}_i} + \frac{1}{2\varepsilon}\hat{\rho}\delta_{i1} + \sqrt{\frac{Pr}{Ra}}\frac{\partial \hat{\sigma}_{ij}}{\partial \hat{x}_j}, \tag{32b}$$

$$\frac{\partial (\hat{\rho}\hat{T})}{\partial \hat{t}} + \frac{\partial \left(\hat{\rho}\hat{u}_j\hat{T}\right)}{\partial \hat{x}_j} = \Lambda\left[-\hat{p}\frac{\partial \hat{u}_j}{\partial \hat{x}_j} + \frac{\gamma}{\Lambda\sqrt{RaPr}}\frac{\partial}{\partial \hat{x}_j}\left(k\frac{\partial \hat{T}}{\partial \hat{x}_j}\right) + \sqrt{\frac{Pr}{Ra}}\hat{\sigma}_{ij}\frac{\partial \hat{u}_j}{\partial \hat{x}_j}\right], \tag{32c}$$

where $\Lambda = \gamma(\gamma-1)Ma^2$, and the z axis is assumed to be in the upward vertical direction. Since the Prandtl number ($Pr = \mu_0 C_p/k_0 = 0.71$) and heat capacity ratio ($\gamma = C_p/C_V = 1.4$) are fixed, the governing parameters for the current problem are Rayleigh number $Ra = \frac{Pr 2\varepsilon g H^3 \rho_0^2}{\mu_0^2}$ and the normalized temperature difference $\varepsilon = \frac{T_h - T_c}{2T_0}$. Parameters of the simulation are shown in Table V. For a set of

TABLE V. Parameters for the simulation of natural convection with a large temperature difference.

Ra	Pr	γ	ε	Ma
1.0×10^6	0.71	1.4	0.6	4.11×10^{-2}
$p_0(\mathrm{kg/ms^2})$	$T_0(\mathrm{K})$	$R(\mathrm{m^2/s^2\,K})$	$g(\mathrm{m/s^2})$	μ_0
101 325.0	600.0	287	$g(Ra)$	0.01

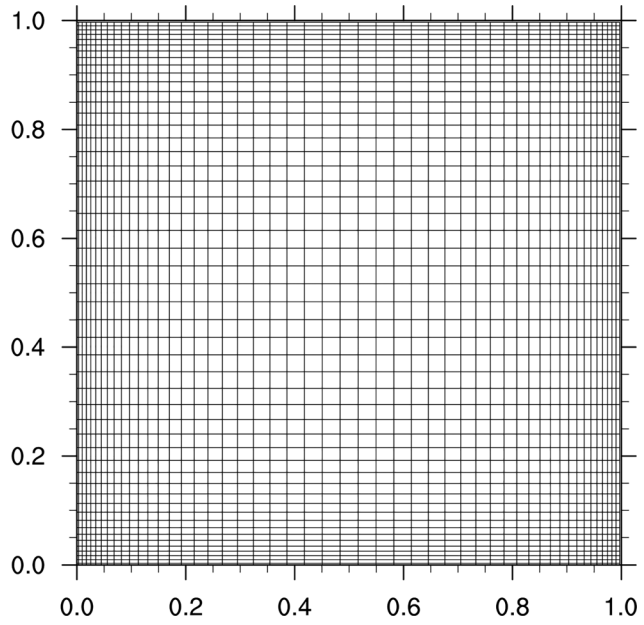

FIG. 2. The mesh layout for the case of $N = 50$ and $S = 3$, as an illustration.

stretched meshes with N grid points in each direction, the location of the cell interfaces $x_b(i)$ is given by

$$x_b(i) = \frac{1}{2}\left[1 + \frac{\tanh[S(i/N - 0.5)]}{\tanh(S/2)}\right], \quad i = 0, 1, 2, \ldots, N, \tag{33}$$

where S is the parameter used to alter the degree of non-uniformity. Then the location of the cell centers can be obtained by $x(i) = [x_b(i) + x_b(i+1)]/2$. The schematic illustration of mesh distribution is shown in Fig. 2. The mesh of the domain is $256 \times 256 \times 2 (S = 3)$ for all simulation cases with $Ra = 1.0 \times 10^6$; non-uniform grids are employed in the vertical (z) and the horizontal (x) direction with the minimum grid space $\Delta x_{min} = 1.182 \times 10^{-3} H$. The time step is determined by the Courant-Friedrichs-Lewy (CFL) condition $\Delta t = CFL \frac{\Delta x_{min}}{U_{max} + \xi_{max}}$ (U_{max} is the maximum flow velocity, and ξ_{max} is the maximum discrete velocity). The CFL number in the current simulation is set to 0.5. The code was run on the National Center for Atmospheric Research's (NCAR-Wyoming) Supercomputer, known as Cheyenne, equipped with 2.3-GHz Intel Xeon E5–2697V4 processors. The computational domain are decomposed in the x-direction, 128 processors are employed for the current case. The wall clock time per step is $4.82 \times 10^{-2} s$, and it takes 1.35×10^7 time steps to obtain the steady results ($u_0 t/H \approx 60$).

The flow at $Ra = 1.0 \times 10^6$, $\varepsilon = 0.6$ is steady. Figure 3 shows isothermal and velocity vector plot (the results of two layers in the y-direction are identical). We can observe that the basic flow feature of compressible natural convection is nicely recovered, thin velocity/thermal boundary layers are developed along the isothermal walls, the temperature is stratified in the cavity center, and the fluid near the hot wall is expanded, while the cold fluid is contracted near the cooled wall.

Figure 4 shows the temperature and velocity profiles at mid-height and mid-width of the cuboid cavity (Pr is added as in the literature $u_0\sqrt{Pr}$ is used as the reference velocity scale). We compare our D3Q77A9 results with the benchmark results of Vierendeels *et al.*[33] using the gas kinetic scheme and also our DUGKS results based on D2Q25A9 results. The D3Q77A9 results reach an excellent agreement with the reference results; this further indicates that the D3Q77A9 model has a ninth degree of precision. The reason for the excellent agreement between the D3Q77A9 model and the D2Q25A9 model will be further explained in Appendix A where we show that the D2Q25A9 model can be viewed as the projection of D3Q77A9 in the 2D space.

Figure 5 shows the Nusselt distribution along the isothermal walls. Non-symmetric distributions are displayed for the hot and cold wall. The Nusselt number is calculated as

$$Nu(z) = \frac{H}{k_0(T_h - T_c)} k \frac{\partial T}{\partial x}\bigg|_{wall} = -\frac{H}{k_0(T_h - T_c)} q_x, \tag{34}$$

where heat flux is defined as $q_x = \frac{1}{2}\int c_x(c^2 g + h) d\boldsymbol{\xi}$. Our D3Q77A9 results agree well with our D2Q25A9 results and other reference results using the conventional CFD methods;[48,49] heat flux is accurately evaluated at the boundary. As we pointed out before that the heat flux evaluation requires fourth-order moments of the equilibrium,

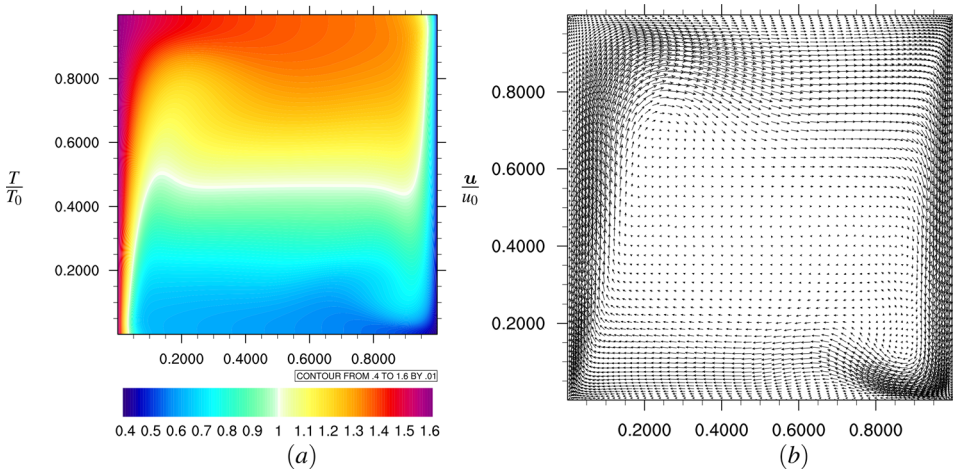

FIG. 3. (a) Isothermal; (b) velocity vector plot for compressible natural convection with $Ra = 1.0 \times 10^6$, $\varepsilon = 0.6$.

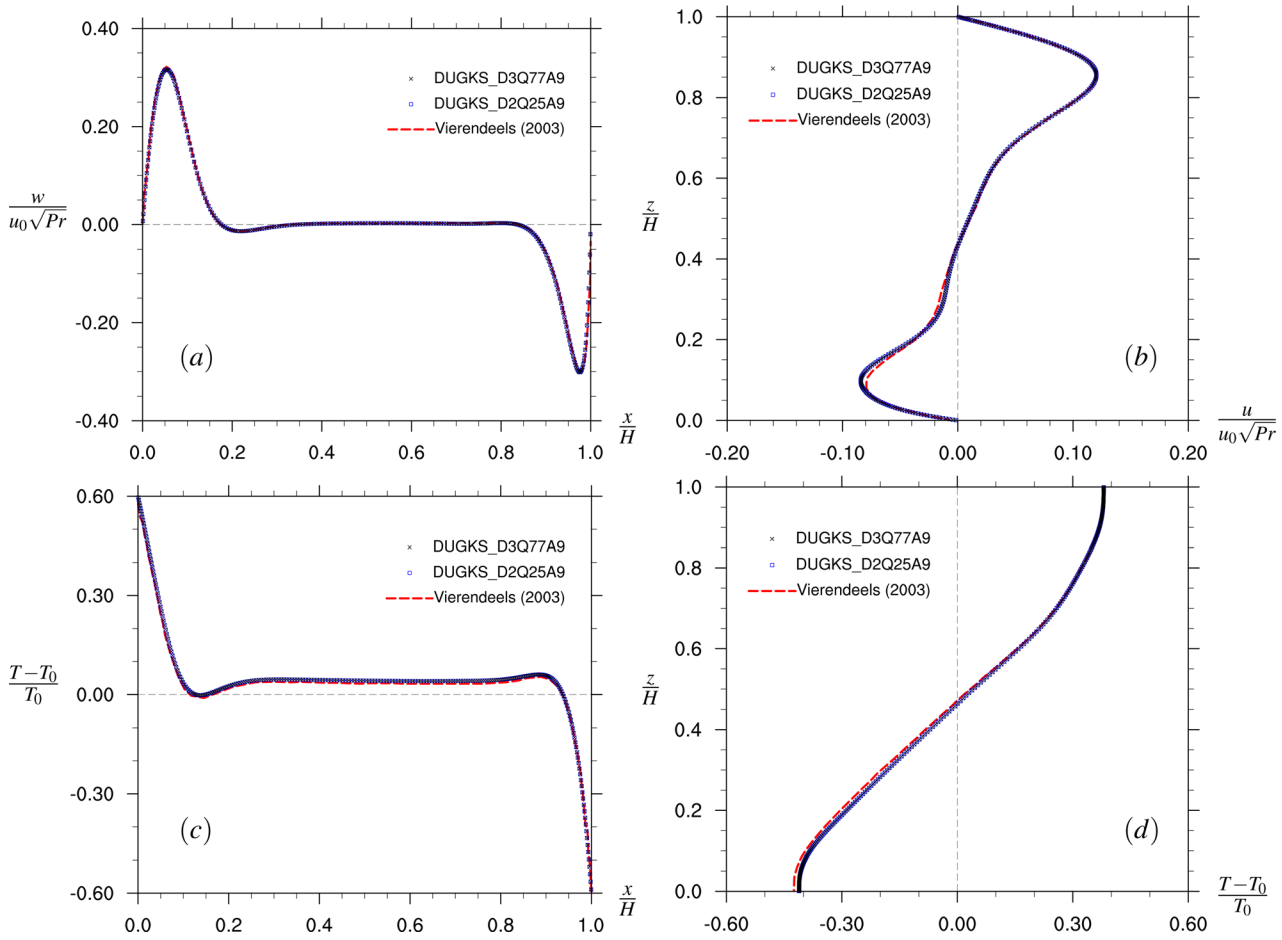

FIG. 4. (a) Vertical velocity $w/(u_0\sqrt{Pr})$ and (c) temperature distribution at the mid-height $z = 0.5H$; (b) horizontal velocity $u/(u_0\sqrt{Pr})$ and (d) temperature distribution at the mid-width $x = 0.5H$ for $Ra = 1.0 \times 10^6$, $\varepsilon = 0.6$.

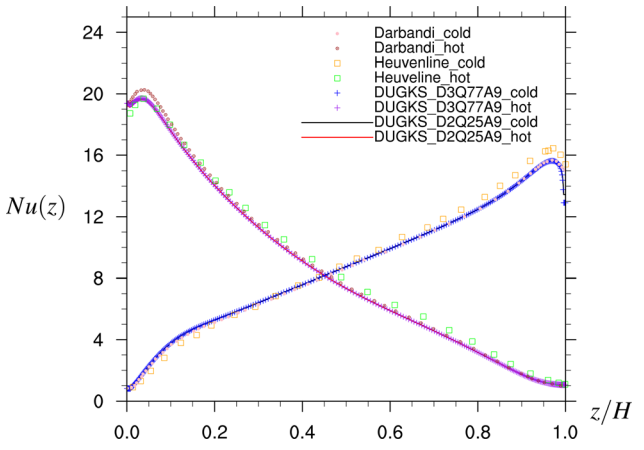

FIG. 5. Nusselt number distribution along the hot and cold walls.

with the fourth-order Hermite expansion of the equilibrium $g^{eq,N=4}$, at least eighth-order quadrature is needed.

B. Three-dimensional natural convection in a cubical cavity

In addition to the above two-dimensional natural convection problem, we next perform three-dimensional simulations of natural convection in a cubical cavity at Rayleigh number $Ra = 1.0 \times 10^3$, for the purpose of validating our 3D compressible DUGKS scheme. We consider an air-filled cubical cavity of height H, with a hot wall at temperature $T_h = T_0(1 + \varepsilon)$ on the left, and a cold wall at temperature $T_c = T_0(1 - \varepsilon)$ on the right. The other four walls (i.e., two other vertical walls and two horizontal walls) are adiabatic. No-slip velocity boundary conditions are imposed on all walls. The mesh of the domain is $50 \times 50 \times 50$, and non-uniform grids with $S = 3$ are introduced in all three directions. Table VI tabulates parameters of the three-dimensional simulations. First, consider the case of $Ra = 1.0 \times 10^3$ and a small temperature difference $\varepsilon = 0.01$. This represents the Boussinesq limit and the flow is steady and symmetric about the cavity

TABLE VI. Parameters for the three-dimensional simulation of natural convection. Parameters in the brackets are for the case with $\varepsilon = 0.6$.

Ra	Pr	γ	ε	Ma
1.0×10^3	0.71	1.4	0.01(0.6)	$1.299 \times 10^{-3}(1.299 \times 10^{-2})$
$p_0(\mathrm{kg/m\,s^2})$	$T_0(\mathrm{K})$	$R(\mathrm{m^2/s^2\,K})$	$g\,(\mathrm{m/s^2})$	μ_0
101 325.0	600.0	287	$g(Ra)$	0.01(0.1)

center. Figure 6 shows the temperature field and the velocity field for natural convection at the mid-plane $y = 0.5H$. The detailed comparisons of the velocity and temperature distribution between the current scheme with a small temperature difference $\varepsilon = 0.01$ and the Boussinesq results are shown in Fig. 7. The Boussinesq flow results are accurately reproduced by the current D3Q77A9 model. Furthermore, the mean Nusselt number distribution $Nu_m(y)$ along the y-direction is shown in Fig. 8. The mean Nusselt number is defined as

$$Nu_m(y) = \frac{1}{H}\int_0^H Nu(y,z)dz, \quad Nu(y,z) = \frac{H}{k_0(T_h - T_c)}k\frac{\partial T}{\partial x}\bigg|_{wall}. \tag{35}$$

Our results agree well with the convectional CFD results of Wang *et al.*,[50] LBM results of Peng *et al.*,[6] and DUGKS results of Wen *et al.*[14] It is worth pointing out that the Nusselt number distribution is sensitive to the boundary treatment. Peng *et al.* used the bounce-back rule of the non-equilibrium distribution function proposed by Zou and He.[51] For the adiabatic wall, they transferred the Neumann boundary condition into the Dirichlet boundary condition by using the finite-difference approximation to obtain the temperature distribution on the wall. Wen *et al.*[14] proposed an improved kinetic boundary condition based on a consistency consideration with the Chapman–Enskog approximation; the Nusselt number distribution is accurately predicted by this boundary treatment. The kinetic boundary condition used in the current study has an accuracy up to $\mathcal{O}(\tau)$, consistent with the derivation of the Navier–Stokes–Fourier equations.

Next, we consider 3D thermal convection with a large temperature difference, namely, $(Ra = 1.0 \times 10^3, \varepsilon = 0.6, \quad Ma = 1.299 \times 10^{-2})$. Figure 9 shows isotherms and velocity vector plot at the mid-plane $y = 0.5H$. With this large temperature difference, the flow is no longer symmetric about the cavity center. The fluid near the hot wall is expanded and that near the cold wall is contracted due to the thermodynamic effect. The center of the flow recirculation moves toward the cold isothermal wall, and the center of the recirculation is shifted to $(x, z) = (0.7050H, 0.4505H)$. The velocity and the temperature profiles at the mid-plane are shown in Fig. 10 and are compared to the profiles in the Boussinesq limit. Clearly, the profiles deviate significantly from the symmetric profiles in the Boussinesq limit. To our knowledge, currently there are no literature data for compressible thermal convection in a 3D cavity, and full discussions of 3D compressible thermal convection flows are beyond the scope of the current paper. Further applications of our DUGKS schemes based on the D3Q77A9 lattice are reported in the work of Chen *et al.*[45,46] for 3D decaying compressible turbulence in a periodic domain for which literature data are widely available.

C. Error analysis

As pointed out by Shan *et al.*,[19] the fourth-order Hermite expansion of the equilibrium distribution function is needed for the heat flux and the energy dynamics to be accurate up to the Navier–Stokes–Fourier level. With the discrete particle velocity space, the requirement translates to fourth-order Hermite expansion of equilibrium and at least eighth-order Gauss–Hermite quadrature. In this study, we shall make a detailed error analysis of inadequate quadrature and Hermite expansion of equilibrium without enough order of expansion. It is worth pointing out that, boundary treatment will enlarge the error, for the thermal flow in an enclosure it is crucial to use appropriate quadrature and equilibrium. A series of simulations with two- and three-dimensional quadrature and third- and fourth-order Hermite expansion of equilibrium g^{eq} are performed to indicate

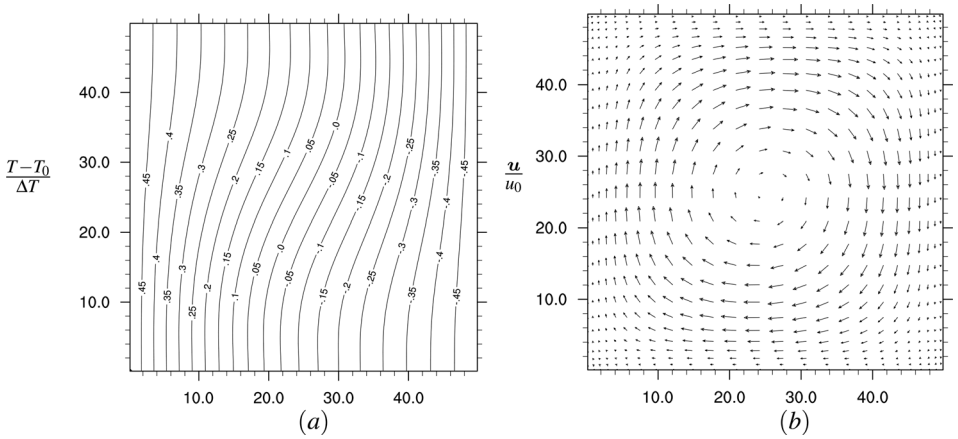

FIG. 6. (a) Isothermal lines and (b) velocity vector plot at the mid-plane $y = 0.5H$ for 3D natural convection at $Ra = 1.0 \times 10^3$ and $\varepsilon = 0.01$. Here the horizontal axis is x and the vertical axis is z.

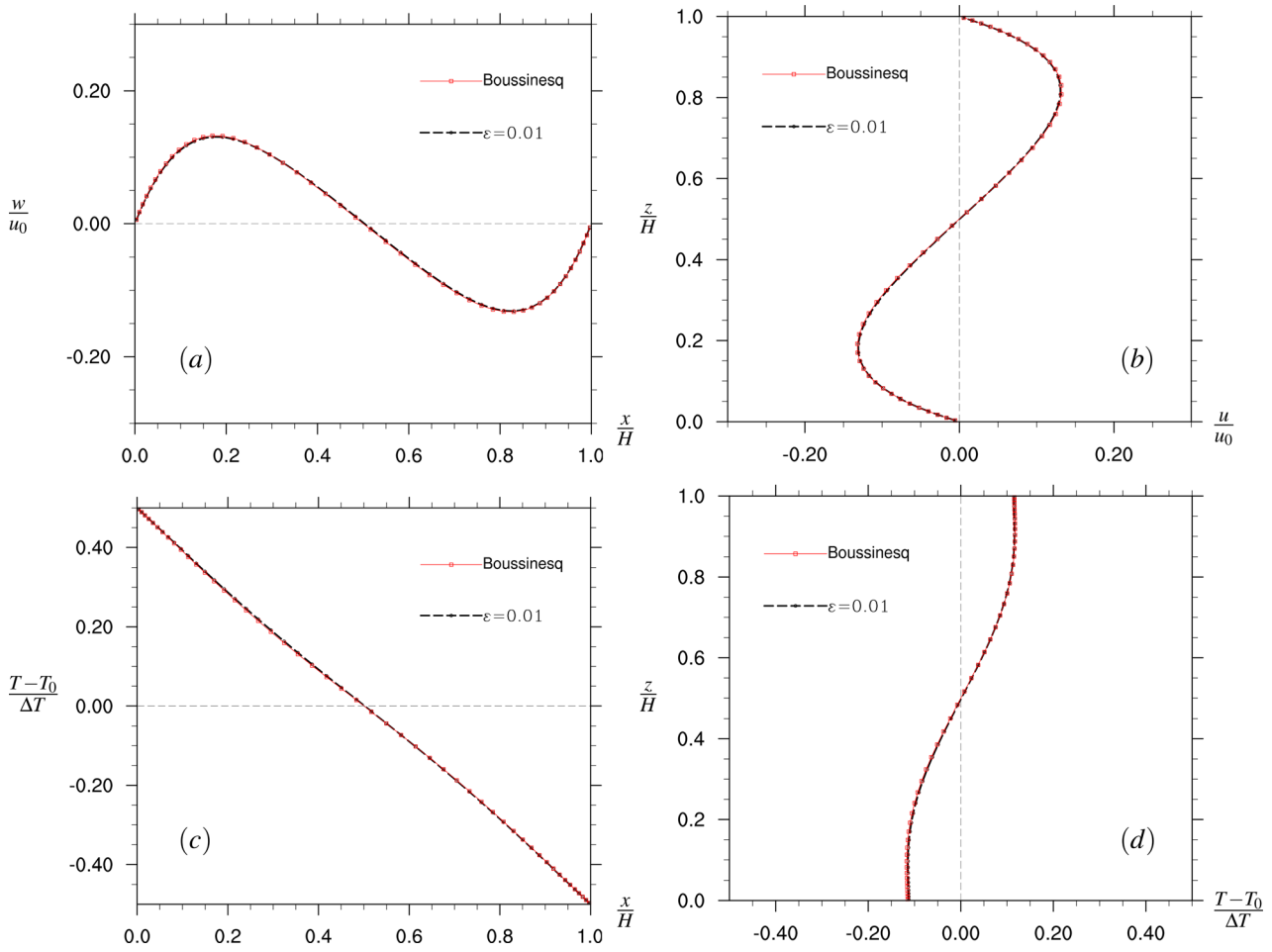

FIG. 7. (a) Vertical velocity w/u_0 and (c) temperature distribution at the mid-height and mid-plane ($z = 0.5H, y = 0.5H$); (b) horizontal velocity u/u_0 and (d). temperature distribution at the mid-width and mid-plane ($x = 0.5H, y = 0.5H$) for $Ra = 1.0 \times 10^3, \varepsilon = 0.01$.

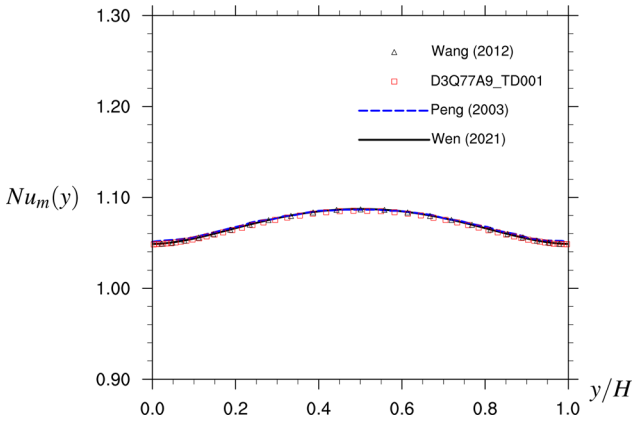

FIG. 8. The distribution of mean Nusselt number $Nu_m(y)$ (averaged over any x-z plane) as a function of the spanwise (y) coordinate.

the magnitude of the error. Table VII shows the quadrature used for simulations, D2Q16A7 and D2Q25A9, are used for two-dimensional simulations, and D3Q27A7 and D3Q77A9 are implemented in the three-dimensional code.

To investigate the influence of inadequate Hermite expansion of equilibrium, the third-order equilibrium $g^{eq,N=3}(\boldsymbol{\xi}_\alpha, \boldsymbol{x}, t)$ is also used in some cases

$$g^{eq,(3)} = \omega_a \rho \left\{ \begin{array}{l} 1 + \dfrac{\xi_{j,a}u_j}{RT_0} + \dfrac{1}{2}\left[\dfrac{(\xi_{j,a}u_j)^2}{(RT_0)^2} - \dfrac{u^2}{RT_0} + (\theta-1)\left(\dfrac{\xi_a^2}{RT_0} - D\right)\right] \\ + \dfrac{1}{6}\dfrac{\xi_{j,a}u_j}{RT_0}\left[\dfrac{(\xi_{j,a}u_j)^2}{(RT_0)^2} - 3\dfrac{u^2}{RT_0} + 3(\theta-1)\left(\dfrac{\xi_a^2}{RT_0} - D - 2\right)\right] \end{array} \right\} + \mathcal{O}(Ma^4). \quad (36)$$

The equilibrium distribution $h^{eq,(2)}$ is expanded to the second order for all simulations. The kinetic boundary treatment is adjusted

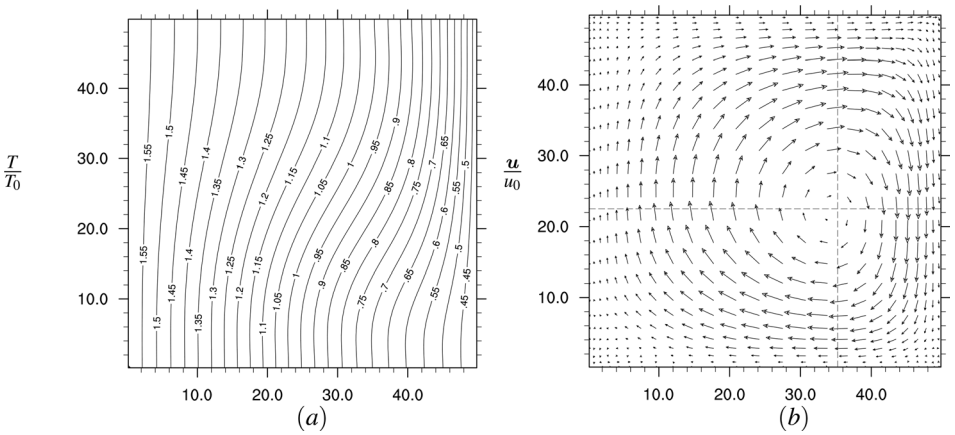

FIG. 9. (a) Isothermal lines and (b) velocity vector plot for natural convection with $Ra = 1.0 \times 10^3, \varepsilon = 0.6$ at the mid-plane $y = 0.5H$. Here the horizontal axis is x and the vertical axis is z.

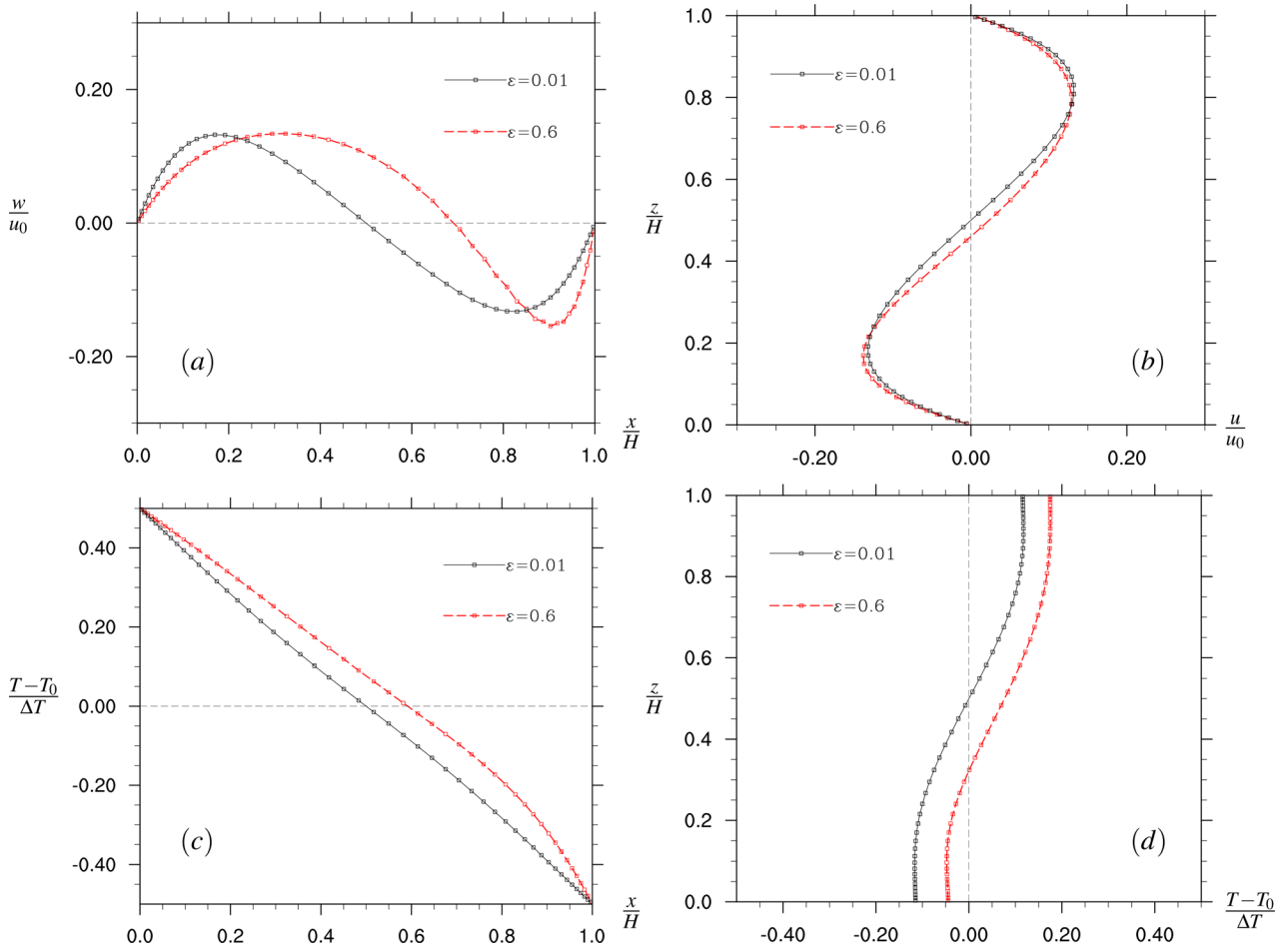

FIG. 10. (a) Vertical velocity w/u_0 and (c) temperature distribution at the mid-height and mid-plane $(z = 0.5H, y = 0.5H)$; (b) horizontal velocity u/u_0 and (d). temperature distribution at the mid-width and mid-plane $(x = 0.5H, y = 0.5H)$ for $Ra = 1.0 \times 10^3, \varepsilon = 0.6$.

TABLE VII. Two- and three-dimensional quadrature. D2Q16A7 and D2Q25A9 are the "production" formulas of D1Q4A7 and D1Q5A9, respectively. D3Q27A7 is derived by Stroud.[52]

Quadrature	$\boldsymbol{\xi}_\alpha$	p	ω_α	
D2Q16A7	(r, r)	4	$(5-2\sqrt{6})/48$	$r^2=(3+\sqrt{6})c_0^2$
	(s, s)	4	$(5+2\sqrt{6})/48$	$s^2=(3-\sqrt{6})c_0^2$
	(r, s)	8	1/48	
D2Q25A9	$(0, 0)$	1	64/225	
	$(r, 0)$	4	$2(7-2\sqrt{10})/225$	$r^2=(5+\sqrt{10})c_0^2$
	$(s, 0)$	4	$2(7+2\sqrt{10})/225$	$s^2=(5-\sqrt{10})c_0^2$
	(r, r)	4	$(89-28\sqrt{10})/3600$	
	(s, s)	4	$(89+28\sqrt{10})/3600$	
	(r, s)	8	1/400	
D3Q27A7	$(0, 0, 0)$	1	$(720+8\sqrt{15})/2205$	
	$(r, 0, 0)$	6	$(270-46\sqrt{15})/15\,435$	$r^2=((15+\sqrt{15})/2)c_0^2$
	$(s, s, 0)$	12	$(162+41\sqrt{15})/6174$	$s^2=(6-\sqrt{15})c_0^2$
	(t, t, t)	8	$(783-202\sqrt{15})/24\,696$	$t^2=(9+2\sqrt{15})c_0^2$

with the expansion order of the equilibrium distribution g^{eq}. For all simulations with the third-order expansion of $g^{eq,(3)}$, the following kinetic boundary condition is used

$$g(\xi_{a,j}) = g(\xi_{\bar{a},j}) - \tau W_a \rho \frac{\xi_j}{T_0}\frac{\partial T}{\partial x_j} \times \left\{ \begin{array}{l} \left(\dfrac{\xi^2}{RT_0} - D - 2\right) \\ \dfrac{1}{2}(\theta-1)\left[\dfrac{\xi_a^4}{(RT_0)^2} - 2(D+3)\dfrac{\xi_a^2}{RT_0} + (D+2)^2\right] \end{array} \right\} + \mathcal{O}(\tau^2, Ma^4). \quad (37)$$

All higher-order terms $\mathcal{O}(Ma^4)$ are neglected and the boundary treatment for $h(\boldsymbol{\xi}_a)$ distribution remains the same. Table VIII shows the various combinations of lattice velocity model and expansion order of the equilibrium distribution g^{eq} as well as the resulting mean temperature of the entire cavity for different cases. Only with ninth-order quadrature and fourth-order Hermite expansion of equilibrium $g^{eq,N=4}$, the correct results can be obtained. With the expansion of the hot fluid, the mean temperature of the cavity is slightly higher than the reference temperature T_0. While for other cases with the seventh degree of precision in the quadrature or third-order Hermite expansion of equilibrium, a large decrease in the mean temperature is observed. The error caused by reduced Hermite expansion order of the equilibrium is more significant than the error caused by the reduced quadrature order.

TABLE VIII. Mean temperature of the cavity for different cases. Dn_1Qn_2An_3Hn_4 indicates the simulation is performed with a n_1-dimensional quadrature with n_2 discrete particle velocities and has a n_3 degree of quadrature precision. The equilibrium g^{eq} is expanded to the n_4-order.

2D	D2Q25A9H4	D2Q25A9H3	D2Q16A7H4	D2Q16A7H3
$\bar{T}/T_0$	1.014 9	0.842 1	0.877 4	0.841 8
3D	D3Q77A9H4	D3Q77A9H3	D3Q27A7H4	D3Q27A7H3
$\bar{T}/T_0$	1.019 2	0.815 3	0.839 5	0.815 2

Figure 11 displays a detailed comparison of temperature and velocity profiles for two-dimensional simulations with different settings. In these two-dimensional simulations, the basic flow features thin boundary layers are developed along the isothermal walls. However, as the heat flux is not evaluated accurately in some cases, the temperature distribution deviates from the benchmark case D2Q25A9H4. As expected, the two cases, D2Q25A9H3 and D2Q16A7H3, with the third-order Hermite expansion of the equilibrium $g^{eq,N=3}$ have similar results. When the g^{eq} equilibrium is expanded to the third order, only seventh-order quadrature is required to evaluate the heat flux, then the two cases D2Q25A9H3 and D2Q16A7H3 should have similar results.

Temperature and velocity profiles from the three-dimensional code are displayed in Fig. 12. Again, only with the ninth degree of precision in the quadrature combined with the fourth-order Hermite expansion of the equilibrium $g^{eq,N=4}$, the correct results can be recovered for the case D3Q77A9H4. Different degree of temperature deviations are observed for other cases, this indicates error appears in the heat flux evaluation. Two cases with the third-order Hermite expansion of equilibrium distribution D3Q77A9H3 and D3Q27A7H3 show similar results.

As shown in Eq. (4), fourth-order moment $\int \xi_i\xi_j\xi^2 g^{eq} d\boldsymbol{\xi}$ is needed to evaluate the heat flux. For instance, with the unexpanded equilibrium distribution $g^{eq} = \frac{\rho}{(2\pi RT)^{D/2}}\exp[-\frac{(\boldsymbol{\xi}-\boldsymbol{u})^2}{2RT}]$, the moments $\int \xi_x\xi_x\xi^2 g^{eq} d\boldsymbol{\xi}$ can be evaluated as

$$\int \xi_x\xi_x\xi^2 g^{eq} d\boldsymbol{\xi} = \rho\left[(D+2)(RT)^2 + (D+4)u_x u_x RT + u^2(RT + u_x u_x)\right]. \quad (38)$$

In the current scheme, the equilibrium distribution is approximated by its Hermite expansion. With the discrete particle velocity space, Gauss–Hermite quadrature is employed for the moments

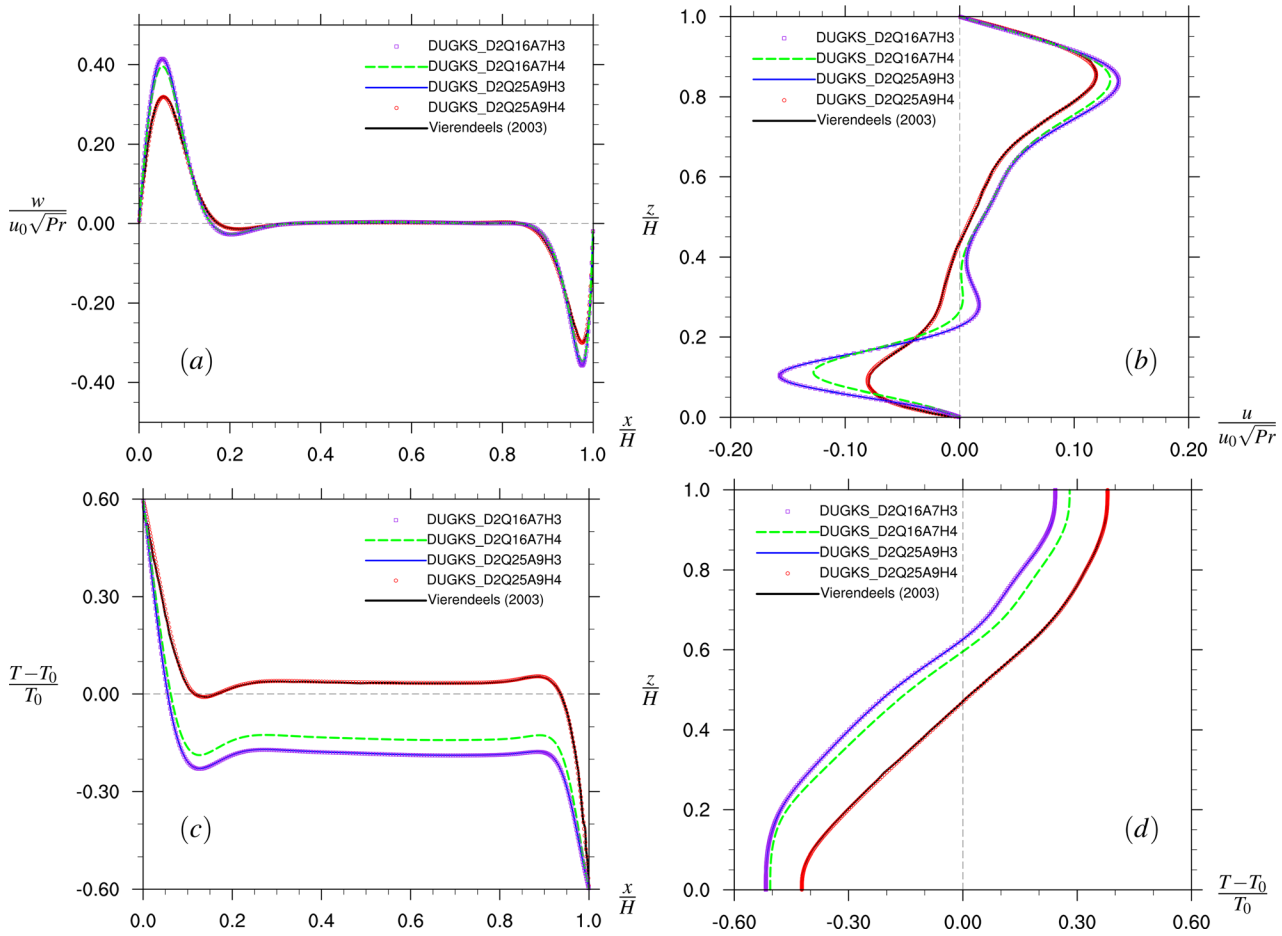

FIG. 11. (a) Vertical velocity $w/(u_0\sqrt{Pr})$ and (c) temperature distribution at the mid-height $z = 0.5H$; (b) horizontal velocity $u/(u_0\sqrt{Pr})$ and (d) temperature distribution at the mid-width $x = 0.5H$ for different two-dimensional cases with $Ra = 1.0 \times 10^6$, $\varepsilon = 0.6$.

evaluation. For the evaluation of the above fourth-order moment, $\int \xi_x\xi_x\xi^2 g^{eq} d\boldsymbol{\xi}$, the fourth-order Hermite expansion of equilibrium $g^{eq,N=4}$ and at least eighth-order quadrature is required to obtain the correct results. Otherwise, errors will be introduced to the heat flux evaluation. Table IX shows the relative error in the fourth-order moment evaluation $\int \xi_x\xi_x\xi^2 g^{eq} d\boldsymbol{\xi}$ for each simulation case, the moments are calculated mesoscopically $\sum_a \xi_{x,a}\xi_{x,a}\xi_a^2 g^{eq}(\boldsymbol{\xi}_a)$ and compared with the macroscopic results [right-hand side of Eq. (38)]. For both two- and three-dimensional ninth order quadrature benchmark cases D2Q25A9H4 and D3Q77A9H4, the fourth-order moment can be evaluated exactly. For other cases, errors of different magnitude start to appear between the moment by mesoscopic calculation and the target value. Furthermore, the boundary treatment will enlarge the error and cause unbalanced heat flux through the isothermal wall which leads to the under-prediction of the mean temperature in the cavity.

It is worth pointing out that the compressibility for the current natural convection problem is due to thermal expansion. The thermal expansion is quantified by the relative temperature difference ε. Due to the low flow speed, the Mach number remains small for the natural convection problem. For the case $Ra = 1.0 \times 10^6$, $\varepsilon = 0.6$, the maximum local Mach number is $Ma_{l,max} \approx 0.0126$, where $Ma_l \equiv \sqrt{u^2 + v^2}/\sqrt{\gamma RT}$. Therefore, Mach number is very small. Thus, the error introduced by inaccurate fourth-order moments evaluation is not due to the Mach number but by the large temperature difference. To verify this hypothesis, we performed another set of two-dimensional simulations with a small temperature difference $\varepsilon = 0.01$ and $Ra = 1.0 \times 10^6$. The parameters for simulations are shown in Table X. Figure 13 shows velocity and temperature profiles for different cases. Unlike the compressible cases, with a small temperature difference $\varepsilon = 0.01$, the reduced Hermite expansion order of equilibrium and the reduced quadrature order do not show any significant effect on the simulation results. All cases reach a good agreement with the Boussinesq benchmark results.

IV. SUMMARY AND CONCLUSIONS

In this paper, we have performed both two-dimensional and three-dimensional simulations of natural convection in a cavity with the discrete unified gas-kinetic scheme. In DUGKS, the Hermite expansion of equilibrium distribution function and Gauss–Hermite

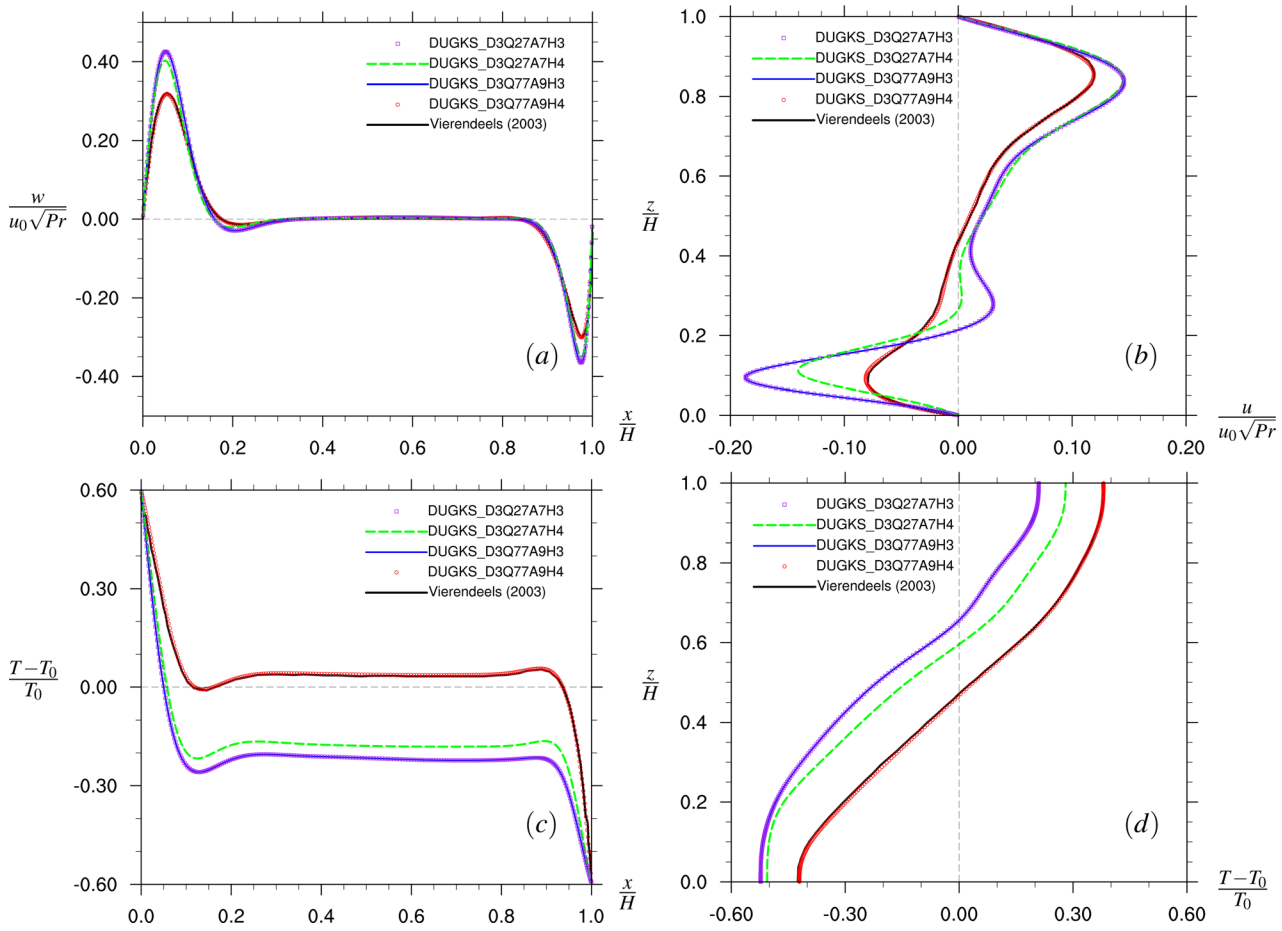

FIG. 12. (a) Vertical velocity $w/(u_0\sqrt{Pr})$ and (c) temperature distribution at the mid-height $z = 0.5H$; (b) horizontal velocity $u/(u_0\sqrt{Pr})$ and (d) temperature distribution at the mid-width $x = 0.5H$ for different three-dimensional cases with $Ra = 1.0 \times 10^6$, $\varepsilon = 0.6$.

TABLE IX. The relative error of the fourth-order moment evaluation $\frac{|Meso-Macro|}{|Macro|}$.

	D2Q25A9H4	D2Q25A9H3	D2Q16A7H4	D2Q16A7H3
Center $\left(\frac{nx}{2}, \frac{nz}{2}\right)$	0.00%	5.06%	2.06%	5.35%
Boundary $\left(0, \frac{nz}{2}\right)$	0.00%	13.89%	10.55%	14.06%
	D3Q77A9H4	D3Q77A9H3	D3Q27A7H4	D3Q27A7H3
Center $\left(\frac{nx}{2}, \frac{nz}{2}\right)$	0.00%	6.32%	3.46%	6.47%
Boundary $\left(0, \frac{nz}{2}\right)$	0.00%	14.16%	11.38%	14.06%

TABLE X. Parameters for the simulation of natural convection with a small temperature difference.

Ra	Pr	γ	ε	Ma
1.0×10^6	0.71	1.4	0.01	4.108×10^{-3}
$p_0(\mathrm{kg/ms^2})$	$T_0(\mathrm{K})$	$R(\mathrm{m^2/s^2\,K})$	$g(\mathrm{m/s^2})$	μ_0
101 325.0	600.0	287	$g(Ra)$	0.001

quadrature are employed as the particle velocity space is discretized. Based on the Chapman–Enskog analysis, fourth-order moments of equilibrium distribution are needed to recover the full Navier–Stokes–Fourier equations. For an accurate compressible thermal flow simulation with the DUGKS, Hermite expansion of the equilibrium to the fourth-order and at least eighth-order Gauss–Hermite quadrature are required. The quadrature D3Q125A9 obtained from the production formula is shown to be redundant for the three-dimensional

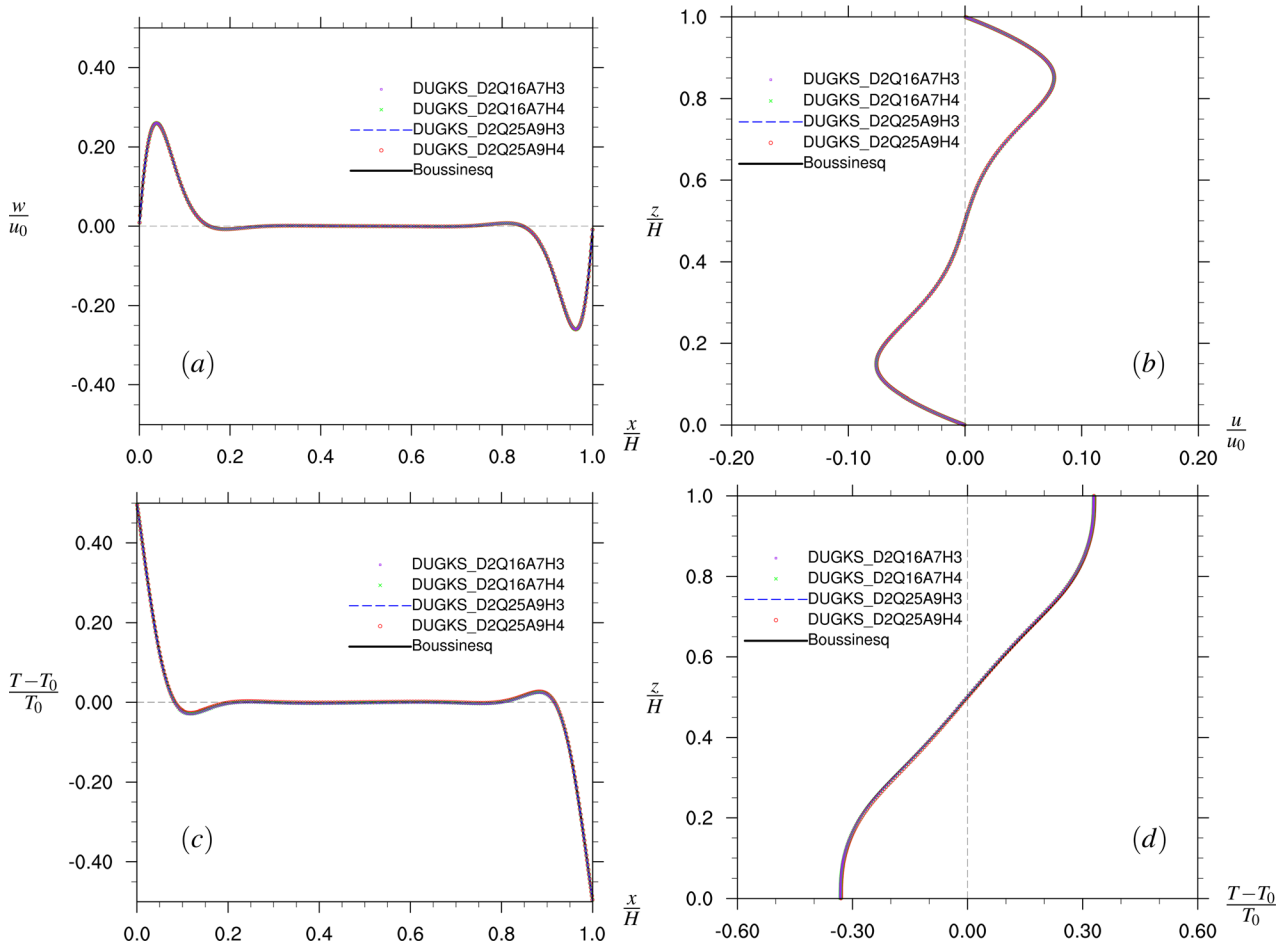

FIG. 13. (a) Vertical velocity w/u_0 and (c) temperature distribution at the mid-height $z = 0.5H$; (b) horizontal velocity u/u_0 and (d) temperature distribution at the mid-width $x = 0.5H$ for $Ra = 1.0 \times 10^6$, $\varepsilon = 0.01$.

simulations. As DUGKS does not require the particle velocity lattice to coincide with the Cartesian grid, we are able to simplify the ninth-order quadrature D3Q125A9 to design a new lattice velocity model D3Q77A9, without losing the degree of precision in the Gauss–Hermite quature. This significantly cuts down the computational cost.

To confirm the accuracy of the D3Q77A9 model, simulations of two-dimensional and three-dimensional compressible natural convection with the D3Q77A9 model are performed. In 2D, the results agree well with our D2Q25A9 results and the literature results. An error analysis is performed to demonstrate the importance of using a quadrature with an adequate degree of precision and the Hermite expansion of equilibrium distribution to an adequate order. A series of simulations with reduced Hermite expansion of equilibrium distribution and reduced quadrature order is performed. The results show that only with ninth-order quadrature and fourth-order Hermite expansion of the equilibrium, the correct results can be obtained for compressible natural convection with a large temperature difference. Errors are introduced by inaccurate evaluation of the fourth-order moments of equilibrium distribution, and this arises when the temperature difference is large. In general, the Mach number of the natural convection flow is small as the compressibility is induced by the temperature difference not by the flow speed. However, our current model is capable of simulating flow with a relatively large Mach number. Chen *et al.*[46] performed simulation of 3D compressible decaying isotropic turbulence using DUGKS with the D3Q77A9 model. They showed that the local maximum Mach number can reach values as high as 1.5.

ACKNOWLEDGMENTS

This work was supported by the National Natural Science Foundation of China (NSFC Award Nos. 91852205, 91741101, 12041601, and 11961131006), NSFC Basic Science Center Program (Award No. 11988102), the U.S. National Science Foundation (Nos. CNS-1513031 and CBET-1706130), the National Numerical Wind Tunnel program, Guangdong Provincial Key Laboratory of

Turbulence Research and Applications (No. 2019B21203001), Guangdong-Hong Kong-Macao Joint Laboratory for Data-Driven Fluid Mechanics and Engineering Applications (No. 2020B1212030001), and Shenzhen Science and Technology Program (Grant No. KQTD20180411143441009). Computing resources are provided by the Center for Computational Science and Engineering of Southern University of Science and Technology and by National Center for Atmospheric Research (No. CISL-UDEL0001).

APPENDIX A: EXAMINATION OF THE DEGREE OF PRECISION FOR D3Q77A9

Starting with the linear system formed by the 11 equations of the D3Q125A9 model, we have shown that it is possible to derive a reduced model, D3Q77A9, of the same quadrature accuracy. To confirm that the D3Q77A9 model provides the ninth degree of precision in the Gauss–Hermite quadrature, we plug the resulting abscissas and weights into the required conditions, Eq. (15). Using the eight reduced velocity groups, we have

$$n=0,\quad \mathscr{H}^{(0)}=1$$
$$w_1+6(w_2+w_3)+12(w_4+w_5)+24w_6+8(w_7+w_8)=1, \tag{A1}$$

$$n=2,\mathscr{H}^{(2)}_{xx}=x^2-1$$
$$-w_1+(2r^2-6)w_2+(2s^2-6)w_3+(8r^2-12)w_4+(8s^2-12)w_5+(8r^2+8s^2-24)w_6+8(r^2-1)w_7+8(s^2-1)w_8=0, \tag{A2}$$

$$n=4,\mathscr{H}^{(4)}_{xxxx}=x^4-6x^2+3$$
$$3w_1+(2r^4-12r^2+18)w_2+(2s^4-12s^2+18)w_3+(8r^4-48r^2+36)w_4+(8s^4-48s^2+36)w_5+(8r^4-48r^2+8s^4-48s^2+72)w_6+8(r^4-6r^2+3)w_7+8(s^4-6s^2+3)w_8=0, \tag{A3}$$

$$n=4,\mathscr{H}^{(4)}_{xxyy}=x^2y^2-(x^2+y^2)+1$$
$$w_1+(-4r^2+6)w_2+(-4s^2+6)w_3+4(r^4-4r^2+3)w_4+4(s^4-4s^2+3)w_5+8\left[r^2s^2-2(r^2+s^2)+3\right]w_6+8(r^4-2r^2+1)w_7+8(s^4-2s^2+1)w_8=0, \tag{A4}$$

$$n=6,\mathscr{H}^{(6)}_{xxxxxx}=x^6-15x^4+45x^2-15$$
$$-15w_1+\left[2(r^6-15r^4+45r^2)-90\right]w_2+\left[2(s^6-15s^4+45s^2)-90\right]w_3+\left[8(r^6-15r^4+45r^2)-180\right]w_4+\left[8(s^6-15s^4+45s^2)-180\right]w_5+\left[8(r^6-15r^4+45r^2)+8(s^6-15s^4+45s^2)-360\right]w_6+8(r^6-15r^4+45r^2-15)w_7+8(s^6-15s^4+45s^2-15)w_8=0 \tag{A5}$$

$$n=6,\mathscr{H}^{(6)}_{xxxxyy}=x^4y^2-(x^4+6x^2y^2)+(6x^2+3y^2)-3$$
$$-3w_1+\left[2(-r^4+9r^2)-18\right]w_2+\left[2(-s^4+9s^2)-18\right]w_3+4(r^6-8r^4+18r^2-9)w_4+4(s^6-8s^4+18s^2-9)w_5+\left[4(r^4s^2+s^4r^2)-8(r^4+s^4+6r^2s^2)+72(r^2+s^2)-72\right]w_6+8(r^6-7r^4+9r^2-3)w_7+8(s^6-7s^4+9s^2-3)w_8=0, \tag{A6}$$

$$n=6,\mathscr{H}^{(6)}_{xxyyzz}=x^2y^2z^2-(x^2y^2+x^2z^2+y^2z^2)+(x^2+y^2+z^2)-1$$
$$-1w_1+6(r^2-1)w_2+6(s^2-1)w_3+12(-r^4+2r^2-1)w_4+12(-s^4+2s^2-1)w_5+24(-r^2s^2+r^2+s^2-1)w_6+8(r^6-3r^4+3r^2-1)w_7+8(s^6-3s^4+3s^2-1)w_8=0, \tag{A7}$$

$$n=8,\mathscr{H}^{(8)}_{xxxxxxxx}=x^8-28x^6+210x^4-420x^2+105$$
$$105w_1+\left[2(r^8-28r^6+210r^4-420r^2)+630\right]w_2+\left[2(s^8-28s^6+210s^4-420s^2)+630\right]w_3+\left[8(r^8-28r^6+210r^4-420r^2)+1260\right]w_4+\left[8(s^8-28s^6+210s^4-420s^2)+1260\right]w_5+\left[8(r^8-28r^6+210r^4-420r^2)+8(s^8-28s^6+210s^4-420s^2)+2520\right]w_6+8(r^8-28r^6+210r^4-420r^2+105)w_7+8(s^8-28s^6+210s^4-420s^2+105)w_8=0, \tag{A8}$$

$$n=8,\mathscr{H}^{(8)}_{xxxxxxyy}=x^6y^2-(x^6+15x^4y^2)+15(x^4+3x^2y^2)-(45x^2+15y^2)+15$$
$$15w_1+(-2r^6+30r^4-120r^2+90)w_2+(-2s^6+30s^4-120s^2+90)w_3+\left[4(r^8-17r^6+75r^4-120r^2)+180\right]w_4+\left[4(s^8-17s^6+75s^4-120s^2)+180\right]w_5+4\left[\begin{array}{l}(r^6s^2+s^6r^2)-(2r^6+2s^6+15r^4s^2+15r^2s^4)\\+30(r^4+s^4+3r^2s^2)-120(r^2+s^2)+90\end{array}\right]w_6+8(r^8-16r^6+60r^4-60r^2+15)w_7+8(s^8-16s^6+60s^4-60s^2+15)w_8=0, \tag{A9}$$

$$n=8,\mathscr{H}^{(8)}_{xxxxyyyy}=x^4y^4-6(x^4y^2+x^2y^4)+(3x^4+3y^4+36x^2y^2)-18(x^2+y^2)+9$$
$$9w_1+(12r^4-72r^2+54)w_2+(12s^4-72s^2+54)w_3+4[r^8-12r^6+48r^4-72r^2+27]w_4+4[s^8-12s^6+48s^4-72s^2+27]w_5+8\left[r^4s^4-6(r^4s^2+r^2s^4)+6(r^4+s^4+6r^2s^2)-36(r^2+s^2)+27\right]w_6+8(r^8-12r^6+42r^4-36r^2+9)w_7+8(s^8-12s^6+42s^4-36s^2+9)w_8=0, \tag{A10}$$

$$n=8,\mathscr{H}^{(8)}_{xxxxyyzz}=x^4y^2z^2-(x^4y^2+x^4z^2+6x^2y^2z^2)+(x^4+6x^2y^2+6x^2z^2+3y^2z^2)-(6x^2+3y^2+3z^2)+3$$
$$3w_1+(2r^4-24r^2+18)w_2+(2s^4-24s^2+18)w_3+4(-2r^6+17r^4-24r^2+9)w_4+4(-2s^6+17s^4-24s^2+9)w_5+\left[-8(r^4s^2+s^4r^2)+8(r^4+s^4+15r^2s^2)-96(r^2+s^2)+72\right]w_6+8(r^8-8r^6+16r^4-12r^2+3)w_7+8(s^8-8s^6+16s^4-12s^2+3)w_8=0. \tag{A11}$$

All the required conditions, obtained based on the 11 independent Hermite polynomial configurations, for the 9th-order quadrature accuracy are indeed satisfied by the abscissas and weights given in the D3Q77A9 model.

As we know, the D3Q125A9 model is obtained from the production formula of the D1Q5A9 model. When we project the D3Q125A9 model onto the 2D plane, we will obtain the D2Q25A9 model. Here, we point out that the project of our D3Q77A9 model also leads to the D2Q25A9 model, namely, the following identities are observed:

$$\omega_{(0,0,0)} + 2\omega_{(r,0,0)} + 2\omega_{(s,0,0)} = \omega_{(0,0)}, \tag{A12a}$$
$$\omega_{(r,0,0)} + 2\omega_{(r,r,0)} + 2\omega_{(r,s,0)} = \omega_{(r,0)}, \tag{A12b}$$
$$\omega_{(s,0,0)} + 2\omega_{(s,s,0)} + 2\omega_{(r,s,0)} = \omega_{(s,0)}, \tag{A12c}$$
$$\omega_{(r,r,0)} + 2\omega_{(r,r,r)} = \omega_{(r,r)}, \tag{A12d}$$
$$\omega_{(s,s,0)} + 2\omega_{(s,s,s)} = \omega_{(s,s)}, \tag{A12e}$$
$$\omega_{(r,s,0)} = \omega_{(r,s)}, \tag{A12f}$$

where the weights on the left indicate the weights of the three-dimensional reduced model (D3Q77A9), and the weights on the right are for the two-dimensional model (D2Q25A9). Each of the above identities can be verified using the results from Tables II and IV.

APPENDIX B: THE CHAPMANENSKOG ANALYSIS

In this section, a Chapman–Enskog analysis is performed to show the requirements of the modified BGK model to recover the Navier–Stokes–Fourier equations. Starting from the modified double distribution BGK models,

$$\frac{\partial g}{\partial t} + \boldsymbol{\xi}\cdot\nabla_{\boldsymbol{x}} g + \boldsymbol{b}\cdot\nabla_{\xi} g = \Omega_g = -\frac{g - g^{eq}}{\tau}, \tag{B1a}$$
$$\frac{\partial h}{\partial t} + \boldsymbol{\xi}\cdot\nabla_{\boldsymbol{x}} h + \boldsymbol{b}\cdot\nabla_{\xi} h = \Omega_h = -\frac{h - h^{eq}}{\tau} + S_h, \tag{B1b}$$
$$S_h = \omega(\boldsymbol{\xi})\left\{\frac{2(1-Pr)q_i}{\tau\sqrt{RT_0}}\frac{\xi_i}{\sqrt{RT_0}}\right\}. \tag{B1c}$$

Integrating Eq. (B1a), we can obtain the continuity equation

$$\int\left[\frac{\partial g}{\partial t} + \boldsymbol{\xi}\cdot\nabla_{\boldsymbol{x}} g + \boldsymbol{b}\cdot\nabla_{\xi} g\right]d\boldsymbol{\xi} = \int \Omega_g d\boldsymbol{\xi}, \tag{B2a}$$
$$\frac{\partial\left(\int g d\boldsymbol{\xi}\right)}{\partial t} + \frac{\partial\left(\int \xi_j g d\boldsymbol{\xi}\right)}{\partial x_j} = 0, \tag{B2b}$$
$$\frac{\partial \rho}{\partial t} + \frac{\partial \rho u_j}{\partial x_j} = 0. \tag{B2c}$$

The continuity equation does not need any closure; therefore, no Chapman–Enskog expansion is needed to recover the continuity equation. For the momentum equation, we integrate Eq. (B1a) with ξ_i

$$\int \xi_i\left[\frac{\partial g}{\partial t} + \xi_j\frac{\partial g}{\partial x_j} + b_j\frac{\partial g}{\partial \xi_j}\right]d\boldsymbol{\xi} = \int \xi_i\Omega_g d\boldsymbol{\xi}, \tag{B3a}$$
$$\frac{\partial\left(\int \xi_i g d\boldsymbol{\xi}\right)}{\partial t} + \frac{\partial\left(\int \xi_i\xi_j g d\boldsymbol{\xi}\right)}{\partial x_j} = \int b_j g d\boldsymbol{\xi}, \tag{B3b}$$
$$\frac{\partial \rho u_i}{\partial t} + \frac{\partial}{\partial x_j}\left(\int \xi_i\xi_j g d\boldsymbol{\xi}\right) = \rho b_j. \tag{B3c}$$

To close Eq. (B3c), Chapman–Enskog expansion of g distribution up to $\mathcal{O}(\tau)$ is needed for the Navier–Stokes level. In this way, third order moments of equilibrium are needed for the viscous term which requires third order Hermite expansion of equilibrium and quadrature with the sixth degree of precision. It is worth pointing out that numerous incompressible LBM simulations use D2Q9A5, D3Q19A5 lattice models which only have a fifth degree of precision which is inadequate in a rigorous sense, unless the model Mach number is kept small (typically the maximum local Mach number should be less than 0.3). A detailed error analysis is needed to examine the error brought by inadequate accuracy order of the quadrature.

For the energy equation, we integrate Eq. (B1a) with ξ^2 and combine with integration of Eq. (B1c)

$$\left\{\begin{aligned}&\int\frac{\xi^2}{2}\left[\frac{\partial g}{\partial t} + \xi_j\frac{\partial g}{\partial x_j} + b_j\frac{\partial g}{\partial \xi_j}\right]d\boldsymbol{\xi}\\ &+\int\frac{1}{2}\left[\frac{\partial h}{\partial t} + \xi_j\frac{\partial h}{\partial x_j} + b_j\frac{\partial h}{\partial \xi_j}\right]d\boldsymbol{\xi}\end{aligned}\right\} = \int(\xi^2\Omega_g + \Omega_h)d\boldsymbol{\xi}, \tag{B4a}$$
$$\frac{\partial}{\partial t}\left[\frac{1}{2}\int(\xi^2 g + h)d\boldsymbol{\xi}\right] + \frac{\partial}{\partial x_j}\left[\frac{1}{2}\int\xi_j(\xi^2 g + h)d\boldsymbol{\xi}\right] = \int b_j\xi_j g d\boldsymbol{\xi}, \tag{B4b}$$
$$\frac{\partial \rho E}{\partial t} + \frac{\partial}{\partial x_j}\left[\frac{1}{2}\int\xi_j(\xi^2 g + h)d\boldsymbol{\xi}\right] = \rho b_j u_j. \tag{B4c}$$

With the Chapman–Enskog expansion of g and h up to $\mathcal{O}(\tau)$, the fourth-order moments of g^{eq} and second-order moments of h^{eq} are needed to realize the energy equation. Thus, based on the analysis above, $g^{eq,N=4}$ and $h^{eq,N=2}$ are used in the current study, and at least an eighth-order quadrature is needed correspondingly.

APPENDIX C: A FEW OTHER POSSIBLE SIMPLIFICATIONS OF D3Q125A9

As shown in Sec. II B, the D3Q125A9 model gives an underdetermined linear system. There are many possible solutions for reducing the linear system. In this section, we make a few other possible choices of eliminating groups: (a) 2 and 3, (b) 4 and 5, (c) 9 and 10, (d) 1 and 6 in Table III. All these other choices lead to a unique system but with some of the weights being negative, and the resulting quadrature models are shown in Tables XI–XIV, respectively. We also confirm that all these models satisfy the general

TABLE XI. Three-dimensional Gauss–Hermite quadrature D3Q113A9, by eliminating groups 2 and 3 in Table III.

Group	$\boldsymbol{\xi}_\alpha$	p	ω_α	
1	$(0, 0, 0)$	1	$2.844\,444\,44 \times 10^{-1}$	
2	$(r, r, 0)$	12	$-3.664\,690\,31 \times 10^{-3}$	$r^2 = (5+\sqrt{10})c_0^2$
3	$(s, s, 0)$	12	$5.255\,357\,92 \times 10^{-2}$	$s^2 = (5-\sqrt{10})c_0^2$
4	$(r, s, 0)$	24	$6.666\,666\,67 \times 10^{-3}$	
5	(r, r, s)	24	$2.911\,180\,41 \times 10^{-3}$	
6	(s, s, r)	24	$-4.994\,513\,74 \times 10^{-3}$	
7	(r, r, r)	8	$-1.015\,470\,60 \times 10^{-3}$	
8	(s, s, s)	8	$3.37658171 \times 10^{-3}$	

TABLE XII. Three-dimensional Gauss–Hermite quadrature D3Q101A9 by eliminating groups 4 and 5 in Table III.

Group	ξ_α	p	ω_α	
1	$(0, 0, 0)$	1	$7.111\,111\,11 \times 10^{-2}$	
2	$(r, 0, 0)$	6	$-2.884\,936\,18 \times 10^{-3}$	$r^2 = (5+\sqrt{10})c_0^2$
3	$(s, 0, 0)$	6	$1.095\,516\,03 \times 10^{-1}$	$s^2 = (5-\sqrt{10})c_0^2$
4	$(r, s, 0)$	24	$4.444\,444\,44 \times 10^{-3}$	
5	(r, r, s)	24	$-4.690\,588\,05 \times 10^{-5}$	
6	(s, s, r)	24	$-9.253\,163\,42 \times 10^{-4}$	
7	(r, r, r)	8	$1.102\,705\,35 \times 10^{-4}$	
8	(s, s, s)	8	$2.558\,417\,39 \times 10^{-2}$	

TABLE XIII. Three-dimensional Gauss–Hermite quadrature D3Q109A9, by eliminating groups 9 and 10 in Table III.

Group	ξ_α	p	ω_α	
1	$(0, 0, 0)$	1	$2.044\,444\,44 \times 10^{-1}$	
2	$(r, 0, 0)$	6	$8.287\,860\,52 \times 10^{-3}$	$r^2 = (5+\sqrt{10})c_0^2$
3	$(s, 0, 0)$	6	$3.171\,213\,95 \times 10^{-2}$	$s^2 = (5-\sqrt{10})c_0^2$
4	$(r, r, 0)$	12	$4.321\,201\,69 \times 10^{-4}$	
5	$(s, s, 0)$	12	$4.493\,825\,02 \times 10^{-2}$	
6	$(r, s, 0)$	24	$-1.574\,074\,07 \times 10^{-3}$	
7	(r, r, s)	24	$-1.52695429 \times 10^{-4}$	
8	(s, s, r)	24	$2.189\,732\,47 \times 10^{-3}$	

TABLE XIV. Three-dimensional Gauss–Hermite quadrature D3Q100A9 by eliminating groups 1 and 6 in Table III.

Group	ξ_α	p	ω_α	
1	$(r, 0, 0)$	6	$8.382\,742\,18 \times 10^{-4}$	$r^2 = (5+\sqrt{10})c_0^2$
2	$(s, 0, 0)$	6	$1.413\,839\,48 \times 10^{-1}$	$s^2 = (5-\sqrt{10})c_0^2$
3	$(r, r, 0)$	12	$2.582\,839\,24 \times 10^{-3}$	
4	$(s, s, 0)$	12	$-1.147\,172\,81 \times 10^{-2}$	
5	(r, r, s)	24	$-2.010\,231\,38 \times 10^{-3}$	
6	(s, s, r)	24	$3.260\,231\,38 \times 10^{-3}$	
7	(r, r, r)	8	$7.821\,764\,16 \times 10^{-4}$	
8	(s, s, s)	8	$2.713\,449\,03 \times 10^{-2}$	

solution, Eq. (15). The appearance of negative weights and larges velocity numbers render these other choices to be undesirable, relative to D3Q77A9.

DATA AVAILABILITY

The data that support the findings of this study are available from the corresponding author upon reasonable request.

REFERENCES

[1]F. J. Alexander, H. Chen, S. Chen, and G. D. Doolen, "Lattice Boltzmann model for compressible fluids," Phys. Rev. A **46**, 1967–1970 (1992).

[2]N. Frapolli, S. S. Chikatamarla, and I. V. Karlin, "Multispeed entropic lattice Boltzmann model for thermal flows," Phys. Rev. E **90**, 043306 (2014).

[3]P. Lallemand and L. S. Luo, "Hybrid finite-difference thermal lattice Boltzmann equation," J. Mod. Phys. B **17**, 41–47 (2003).

[4]P. Lallemand and L. S. Luo, "Theory of the lattice Boltzmann method: Acoustic and thermal properties in two and three dimensions," Phys. Rev. E **68**, 036706 (2003).

[5]X. Y. He, S. Y. Chen, and G. D. Doolen, "A novel thermal model for the lattice Boltzmann method in incompressible limit," J. Comput. Phys. **146**, 282–300 (1998).

[6]Y. Peng, C. Shu, and Y. T. Chew, "A 3D incompressible thermal lattice Boltzmann model and its application to simulate natural convection in a cubic cavity," J. Comput. Phys. **193**, 260–274 (2004).

[7]Y. Shi, T. S. Zhao, and Z. L. Guo, "Thermal lattice Bhatnagar-Gross-Krook model for flows with viscous heat dissipation in the incompressible limit," Phys. Rev. E **70**, 066310 (2004).

[8]Z. L. Guo, C. Zheng, B. C. Shi, and T. S. Zhao, "Thermal lattice Boltzmann equation for low Mach number flows: Decoupling model," Phys. Rev. E **75**, 036704 (2007).

[9]Y. L. Feng, P. Sagaut, and W. Q. Tao, "A three dimensional lattice model for thermal compressible flow on standard lattices," J. Comput. Phys. **303**, 514–529 (2015).

[10]X. W. Shan, "Simulation of Rayleigh-Bénard convection using a lattice Boltzmann method," Phys. Rev. E **55**, 2780–2788 (1997).

[11]K. Xu and S. H. Lui, "Rayleigh-Bénard simulation using the gas-kinetic Bhatnagar-Gross-Krook scheme in the incompressible limit," Phys. Rev. E **60**, 464–470 (1999).

[12]J. Wang, D. Wang, P. Lallemand, and L. S. Luo, "Lattice Boltzmann simulation of thermal convective flow in two dimensions," Comput. Math. Appl. **65**, 262–286 (2013).

[13]A. Xu, L. Shi, and H. D. Xi, "Lattice Boltzmann simulations of three-dimensional thermal convective flows at high Rayleigh number," Int. J. Heat Mass Transfer **140**, 359–370 (2019).

[14]X. Wen, L. P. Wang, Z. L. Guo, and D. B. Zhakebayev, "Laminar to turbulent flow transition inside the boundary layer adjacent to isothermal wall of natural convection flow in a cubical cavity," Int. J. Heat Mass Transfer **167**, 120822 (2021).

[15]H. N. Dixit and V. Babu, "Simulation of high Rayleigh number natural convection in a square cavity using the lattice Boltzmann method," Int. J. Heat Mass Transfer **49**, 727–739 (2006).

[16]L. H. Hung and J. Y. Yang, "A coupled lattice Boltzmann model for thermal flows," IMA J. Appl. Math. **76**, 774–789 (2011).

[17]Z. L. Guo, K. Xu, and R. J. Wang, "Discrete unified gas kinetic scheme for all Knudsen number flows. 2. Thermal compressible case," Phys. Rev. E **91**, 033313 (2015).

[18]X. Wen, L. P. Wang, Z. L. Guo, and J. Shen, "An improved discrete unified gas kinetic scheme for simulating compressible natural convection flows," J. Comput. Phys. **11**, 100088 (2021).

[19]X. W. Shan, X. F. Yuan, and H. D. Chen, "Kinetic theory representation of hydrodynamics: A way beyond the Navier-Stokes equation," J. Fluid Mech. **550**, 413–441 (2006).

[20]K. Xu, "A gas-kinetic BGK scheme for the Navier-Stokes equations and its connection with artificial dissipation and Godunov method," J. Comput. Phys. **171**, 289–335 (2001).

[21]S. Lenz, M. Krafczyk, M. Geier, S. Z. Chen, and Z. L. Guo, "Validation of a two-dimensional gas-kinetic scheme for compressible natural convection on structured and unstructured meshes," Int. J. Therm. Sci. **136**, 299–315 (2019).

[22]K. Xu and J. C. Huang, "A unified gas-kinetic scheme for continuum and rarefied flows," J. Comput. Phys. **229**, 7747–7764 (2010).

[23]Z. L. Guo, K. Xu, and R. J. Wang, "Discrete unified gas kinetic scheme for all Knudsen number flows: Low-speed isothermal case," Phys. Rev. E **88**, 033305 (2013).

[24]P. Wang, S. Tao, and Z. L. Guo, "A coupled discrete unified gas-kinetic scheme for Boussiensq flows," Comput. Fluids **120**, 70–81 (2015).

[25]P. Wang, Y. H. Zhang, and Z. L. Guo, "Numerical study of three-dimensional natural convection in a cubical cavity at high Rayleigh numbers," Int. J. Heat Mass Transfer **113**, 217–228 (2017).

[26]L. H. Zhu, P. Wang, and Z. L. Guo, "Performance evaluation of the general characteristic based off-lattice Boltzmann scheme and DUGKS for low speed continuum flows," J. Comput. Phys. **333**, 227–246 (2017).
[27]P. Wang, L. H. Zhua, Z. L. Guo, and K. Xu, "A comparative study of LBE and DUGKS methods for nearly incompressible flows," Commun. Comput. Phys. **17**, 657–681 (2015).
[28]Y. T. Bo, P. Wang, Z. L. Guo, and L. P. Wang, "DUGKS simulations of three-dimensional Taylor-Green vortex flow and turbulent channel flow," Comput. Fluids **155**, 9–21 (2017).
[29]P. L. Quéré and M. Behnia, "From onset of unsteadiness to chaos in a differentially heated square cavity," J. Fluid Mech. **359**, 81–107 (1998).
[30]S. Paolucci and D. R. Chenoweth, "Transition to chaos in a differentially heated vertical cavity," J. Fluid Mech. **201**, 379–410 (1989).
[31]S. Paolucci, "On the filtering of sound from the Navier-Stokes equations," Sandia National Laboratories Report SAND82-8257, 1982.
[32]J. Vierendeels, B. Merci, and E. Dick, "Numerical study of natural convective heat transfer with large temperature differences," Int. J. Numer. Method Heat Fluid Flow **11**, 329–341 (2001).
[33]J. Vierendeels, B. Merci, and E. Dick, "Benchmark solutions for the natural convective heat transfer problem in a square cavity with large horizontal temperature differences," Int. J. Numer. Method Heat Fluid Flow **13**, 1057–1078 (2003).
[34]D. R. Chenoweth and S. Paolucci, "Natural convection in an enclosed vertical air layer with large horizontal temperature differences," J. Fluid Mech. **169**, 173–210 (1986).
[35]P. L. Quéré, R. Masson, and P. Perrot, "A Chebyshev collocation algorithm for 2D non-Boussinesq convection," J. Comput. Phys. **103**, 320–335 (1992).
[36]P. L. Quéré, C. Weisman, H. Paillére, J. Vierendeels, E. Dick, R. Becker, M. Braack, and J. Jocke, "Modeling of natural convection flows with large temperature differences: A benchmark problem for low Mach number solvers. Part 1. Reference solutions," ESAIM: Math. Modell. Numer. Anal. **39**, 609–616 (2005).
[37]H. Paillére, P. L. Quéré, C. Weisman, J. Vierendeels, E. Dick, M. Braack, F. Dabbene, A. Beccantini, E. Studer, T. Kloczko, C. Corre, V. Heuveline, M. Darbandi, and S. F. Hosseinizadeh, "Modeling of natural convection flows with large temperature differences: A benchmark problem for low Mach number solvers. Part 2. Contribution to the June 2004 conference," ESAIM: Math. Modell. Numer. Anal. **39**, 617–621 (2005).
[38]R. Becker and M. Braack, "Solution of a stationary benchmark problem for natural convection with large temperature difference," Int. J. Therm. Sci **41**, 428–439 (2002).
[39]Q. Li, K. H. Luo, Y. L. He, and W. Q. Tao, "Coupling lattice Boltzmann model for simulation of thermal flows on standard lattices," Phys. Rev. E **85**, 016710 (2012).
[40]Y. L. Feng, S. L. Guo, W. Q. Tao, and P. Sagaut, "Regularized thermal lattice Boltzmann method for natural convection with large temperature differences," Int. J. Heat Mass Transfer **125**, 1379–1391 (2018).
[41]E. M. Shakhov, "Generalization of the Krook kinetic relaxation equation," Fluid Dyn. **3**, 95–96 (1968).
[42]L. H. Holway, "New statistical model for kinetic theory: Method of construction," Phys. Fluids **9**, 1658 (1968).
[43]X. W. Shan, "General solution of lattices for Cartesian lattice Bhatanagar-Gross-Krook models," Phys. Rev. E **81**, 036702 (2010).
[44]X. W. Shan, "The mathematical structure of the lattices of the lattice Boltzmann method," J. Comput. Sci. **17**, 475–481 (2016).
[45]T. Chen, X. Wen, L. P. Wang, Z. L. Guo, J. C. Wang, and D. B. Zhakebayev, "Simulation of three-dimensional forced compressible isotropic turbulence by a redesigned discrete unified gas kinetic scheme," J. Comput. Phys. (submitted) (2020).
[46]T. Chen, X. Wen, L. P. Wang, Z. L. Guo, J. C. Wang, and S. Y. Chen, "Simulation of three-dimensional compressible decaying isotropic turbulence using a redesigned discrete unified gas kinetic scheme," Phys. Fluids **32**, 125104 (2020).
[47]H. Grad, "Note on N-dimensional Hermite polynomials," Commun. Pure Appl. Math. **2**, 325 (1949).
[48]M. Darbandi and S. F. Hosseinizadeh, "General pressure-correction strategy to include density variation in incompressible algorithms," AIAA J. Thermophys. Heat Transfer **17**, 372–280 (2003).
[49]V. Heuveline, "On higher-order mixed FEM for low Mach number flows: Application to a natural convection benchmark problem," Int. J. Numer. Method Fluids **41**, 1339–1356 (2003).
[50]C. A. Wang, H. Sadat, and C. Prax, "A new meshless approach for three dimensional fluid flow and related heat transfer problems," Comput. Fluids **69**, 136–146 (2012).
[51]Q. S. Zou and X. Y. He, "On pressure and velocity boundary conditions for the lattice Boltzmann BGK model," Phys. Fluids **9**, 1591–1598 (1997).
[52]A. H. Stroud, *Approximate Calculation of Multiple Integrals* (Prentice-Hall, 1971).